Development And Optimization Of An Intrinsic Optical Signal Imaging System For Hemodynamic Correction Of Fluorescent Signals

By

Aaron T. Cherian

B.S., University of Maryland, College Park, 2018

Thesis

Submitted in partial fulfillment of the requirements for the
Degree of Master of Science in Biomedical Engineering at Brown University

PROVIDENCE, RHODE ISLAND

MAY 2020

This thesis by Aaron T. Cherian is accepted in its present form by the Center of Biomedical Engineering as satisfying the thesis requirement for the degree of Master of Science.

Date Apr 28, 2020

Jonghwan Lee, PhD, Advisor

Recommended to the Graduate Council

Date Apr 27, 2020

Kimani Toussaint, PhD, Reader

Date Apr 27, 2020

Marissa Gray (Apr 27, 2020)

Marissa Gray, PhD, Reader

Approved by the Graduate Council

Date Apr 27, 2020

Marissa Gray (Apr 27, 2020)

Dr. Marissa Gray, Biomedical Engineering Master's Program Director

ACKNOWLEDGEMENTS

This has been a long ride and I owe a lot to the people who have helped me through it. First and foremost to my parents, without them I would not have had the chance to be here in the first place, and I'm incredibly fortunate to have them. To my family, who has always supported me, thank you.

A big thank you to my advisor, Dr. Jonghwan Lee, who even as busy as he was always took the time to meet with and guide me forwards in my research. I look forward to what the Lee Lab will produce in the coming years. Thanks to my committee, Dr. Kimani Toussaint and Dr. Marissa Gray for the time that they took out to read my thesis and attend my defense, and particular thanks to Dr. Gray for her guidance as the masters program director over the past couple of years. Thanks to Sabina Stefan in the Lee Lab, for getting me up to speed on our lab and being there for any and all questions I had. I would have gone crazy without her help

Thank you to all my friends who've been keeping me sane for the past couple of years. I've built up a strong support network here and I'm always thankful for it. And a final thank you to the Brown University at large, students and faculty who have been there, for your inclusiveness, creativity and kindness.

Table of Contents

LIST OF FIGURES

1 AGE RELATED MACULAR DEGENERATION (AMD)

1.1 DISEASE OVERVIEW

Age-related macular degeneration (AMD) is a degenerative disorder of the eye that leads to visual impairment, and in some cases, blindness. Among elderly patients, AMD is one of the leading causes of blindness[1]. The disease is associated with the development of lipid deposits called drusen under the retina[2]. The formation of drusen has been associated with thinning of the macula, which can cause loss of function that results in central vision loss[2]. AMD can be categorized as one of two types: dry or wet.

Associated with late stage AMD is thinning of the retinal pigmental epithelium (RPE), which is involved in transport of nutrients to maintain photoreceptor visual function. Photoreceptor visual function is to transduce light into signals that can be sent down the visual cortex pathway[3]. During late stage dry AMD, in what is known as geographic atrophy, thinning of the RPE can lead to loss of photoreceptors, causing blind spots, and eventually, all central vision. While dry AMD accounts for most diagnosed cases of the disease, in some cases it can also progress to wet AMD, which is associated with severe vision loss. Wet AMD is mainly defined by choroidal neovascularization (CNV), in which new vessels penetrate Bruch's membrane, part of the vascular layer of the eye, and grow into the subretinal space, which can leak fluid or blood[1]. Wet type AMD can lead to severe and rapid vision loss if left untreated.

1.2 Risk Factors And Epidemiology

AMD is the leading cause of irreversible blindness in the US[6]. In 2000, about 1.75 million Americans had late stage AMD, while 7.3 million more were estimated to have early stages of the disease[4].

1.2.1 Age

Age has been found to be the strongest risk factor for AMD[5,6]. In the Beaver Eye Dam population study, incidence of early AMD was found to increase from 3.9% for individuals in the 43-54 year old age range to 22.8% for individuals 75 and older[7]. According to the U.S. Census Bureau in its 2017 National Population Projections, 49.2 million Americans were 65 years or older in 2016, and that number is projected to rise to 94.7 million by 2060[8]. With the increase in elderly population, it becomes even more likely that the prevalence of AMD will continue to increase as well. One study projects the number of global cases of AMD to be 196 million in 2020 and for that to rise to 288 million by 2040[9]. Another study by Rein et. all projects that in the U.S., early AMD incidence will increase to approximately 17.8 million in 2050, as seen in Figure 1[10].

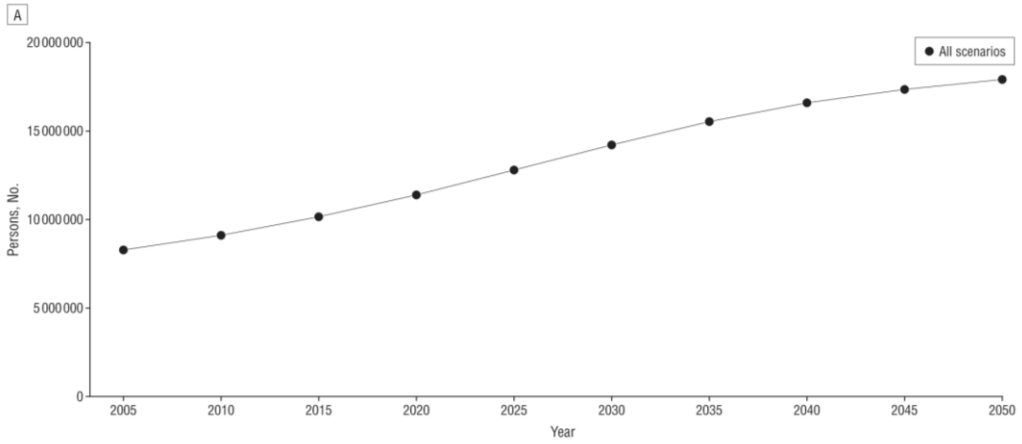

Figure 1: Projection of U.S. AMD incidence, 2005-2050. Source: Rein et. all[12]

1.2.2 Quality of Life

For both wet and dry AMD, there are no clinical treatments that can significantly reverse vision loss and most treatments manage symptoms by slowing disease progression. Therefore, many elderly patients must adjust to impaired or total loss of vision. One study found that of a surveyed group of elderly patients with AMD, 32.5% had some sort of depressive disorder, and severity of depressive symptoms were also closely correlated with disability scores, with the ultimate conclusion that more strategies were needed to help patients cope with vision loss[11]. An intervention that restores vision to AMD patients would be instrumental in increasing their overall quality of life.

1.3 Current Treatments

1.3.1 Vitamin Therapy

A high antioxidant and zinc diet during the early stages of AMD has been found to be effective in reducing risk of CNV and geographic atrophy, the most vision threatening symptoms of both types of AMD. A combination of vitamins termed AREDS2, recommended by the National Eye Institute, can be bought over the counter at local pharmacies, and has been found to be a cost effective AMD treatment[12]. However, vitamin therapy, while slowing the progression of the disease, cannot reverse any vision already lost.

1.3.2 Implantable Mini Telescope

The implantable miniature telescope (IMT), by CentraSight, is the first device approved as a therapy for patients with late stage AMD. The device is implanted in one eye and uses wide-angle micro optics to project a magnified image over the central retina. With the implantation of the IMT, one eye provides central vision, while the other eye provides peripheral vision [13].

The results from the IMT so far have been promising, showing a significant increase in best-corrected visual acuity scores, with a benefit that was sustained over two years despite the progressive

nature of AMD[14]. A 12.5% quality of life gain was reported for the average patient implanted with the IMT[15]. However, the IMT cannot be implanted in every patient and involves a complicated surgery and recovery process.

1.3.3 CONCLUSIONS

For people diagnosed with dry late stage AMD, there are few effective restorative options, and most current treatment is based around managing the progression of systems. For this reason, a growing field in restorative solutions is creating retinal prosthetics, expanded upon in Chapter 2.

2 Chapter 2: Retinal Prosthetics As An AMD Treatment

2.1 Retinal Prosthetic Overview

The general goal of visual prosthetics is to bypass failing parts of the visual pathway and use intact pathways to restore sight. Visual prosthetics generally follow a certain architecture that consist of an external unit to capture, process and send the image while the implanted unit receives and processes the data, before directing a micro-electrode array to stimulate the tissue that it interfaces with (Figure 2)[16].

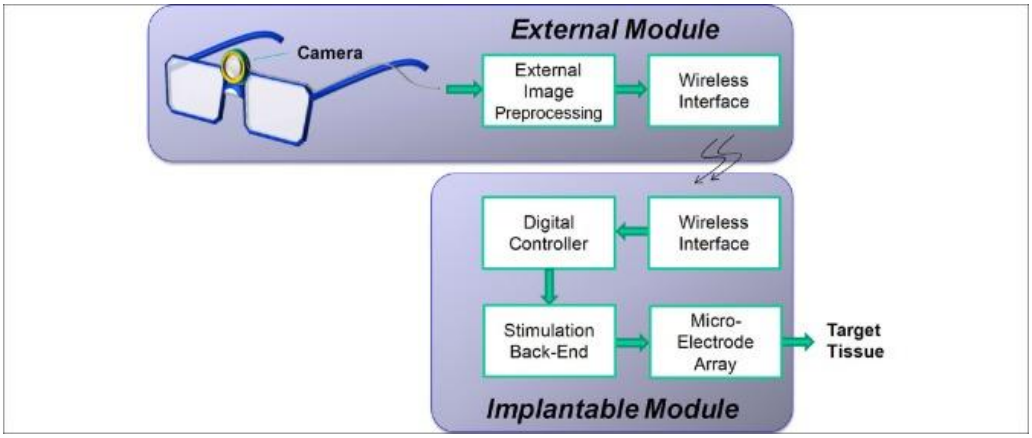

Figure 2: General Architecture of Visual Prosthetics. Source: Maghami et. all[23]

Quality of the image seen by the patient is most heavily dependent on the resolution of the image delivered to the visual system. Resolution is limited by the number of the electrodes on the array (and by extension the number of stimulation sites on the tissue)[17].

2.2 Retinal Prosthetics of Note

2.2.1 Second Sight, the Argus II and the Orion

Second Sight, a U.S. based company focused on neurostimulation technology has developed/is developing two retinal prosthetics systems for dry AMD patients. The Argus II retinal prosthetic, by

Second Sight, was the first approved clinical prosthetic. The Argus II consists of a 60-electrode array surgically implanted in the epiretinal space, electrically stimulating retinal ganglion cells. Long-term studies showed improvements in visual tasks and stable visual performance[25]. The Argus II was initially marketed towards patients with retinitis pigmentosa, a hereditary disease that results in the loss of peripheral vision. After entering market, Second Sight announced in 2015 that they had successfully implanted the Argus II in a late-stage dry AMD patient as part of a feasibility study[26].

In 2019, production on the Argus II was suspended as Second Sight shifted to focus their efforts on the Orion Visual Cortical Prosthesis System[28]. This prosthetic system bypasses a retinal implant entirely by transmitting electrical signals to an array of electrodes implanted on the surface of the brain's visual cortex, with an early feasibility trial currently running.

2.2.2 Pixium Prima

Another frontrunner in development is the photovoltaic retinal implant (PRIMA) bionic vision system by Pixium. PRIMA uses a novel method of photovoltaic stimulation. A chip with 142-pixel cells is implanted into the subretinal space. Pulsed near infrared light stimulates the pixels, and the photodiodes generate a current to polarize neuronal tissue. Results published by the group show that non-human primates responded to stimulations at the implant site and that the implant can remain stable in the retina[29]. In January 2020, the first successful implantation of a patient in the US was completed, one of five planned for a US feasibility study[30].

2.3 LIMITATIONS

The main limitations of treatments for dry AMD can be categorized as restoration, resolution, and invasiveness. Market treatments like vitamin therapy are not restorative, while options like retinal prosthetics are low resolution, and the IMT, while higher resolution and restorative, is extremely invasive.

2.3.1 RESTORATION

Most clinically approved dry AMD treatment is based around managing symptoms. While vitamin therapy is a cost-effective disease treatment, it cannot restore vision. Restoring vision to patients would give them back independence to safely perform tasks, decreasing caregiver costs, and generally improving quality of life. The IMT can restore vision to a patient, but there are drawbacks, which are described in the Invasiveness section below.

2.3.2 RESOLUTION

Generally, the quality of sight restored by retinal prosthetics is extremely low resolution[17]. Devices are not intended to restore vision back to pre-AMD levels but to restore some sense of object recognition and functionality to patients. Patients perceive vision as patterns of light, with some added contrast sensitivity. Resolution is primarily based on the number of sites on the retina that can be stimulated, which is limited by the electrode density in the array. Electrode density is constrained by additional demands placed on the implanted array. Requirements that the array be permanently implanted in the eye increases packaging for the implant to increase safety and longevity, but decreases the space available for a microelectrode array[17].

2.3.3 INVASIVENESS

All available/developing prosthetics require surgery for implantation in the retina, with the extensiveness of the surgery depending on where the implantation site is. Surgeries create increased

risk to the patient, both from surgical complications, and the risk of implant failure and removal. They also create an increased healthcare burden due to surgeon, surgery, and recovery costs.

2.4 Project Goal and Thesis Scope

These limitations leave a space for a minimally invasive, high resolution retinal prosthetic. As such, one novel method of doing this is through optical stimulation. Pulses of NIR light have been previously shown in research to evoke neural responses from neurons[18,19]. This novel method presents a way to stimulate the neurons with a retinal prosthetic. A key part of this process going forward is proving that NIR optical stimulation produces a response in the visual cortex of the brain. We plan on doing so using wide-field calcium imaging of the brain. This thesis focuses on the specifics of the kind of calcium imaging being used, the issues that must be noted, and how we can correct for those issues.

3 Chapter 3: Imaging the Brain

3.1 Calcium Activity As A Proxy For Neural Activity

Calcium is a crucial intracellular messenger that plays an important role in multiple cell functions, including signal flow[20]. In the nervous system, calcium has a number of specific functions, such as trigging release of synaptic vesicles, playing a role in synaptic plasticity, and even regulating gene transcription[21]. Calcium activity can also be associated with triggering action potentials. Action potential signals open calcium channels in the membrane, leading to a calcium influx, and the timing of action potentials has been linked to dendritic spikes of calcium[22,23]. Therefore, by tracking calcium activity, one can also track neural activity.

3.2 Imaging Calcium Activity in the Brain

Fluorescence imaging of the brain has been developed as a nondestructive, temporally and spatially high resolution method to track neural activity, having advantages in sensitive and applicability over absorbance imaging[24]. Early experiments using fluorescence imaging to track neural activity were typically done in insects and lower vertebrates, such as imaging of the brain of a honeybee after olfactory stimulation[25,26]. Initial fluorescent indicators were synthetic molecules such as Quin-2, Fura-2, Indo-1 and Fluo-3[24].

Two main classes of fluorescent indicators exist, expanded upon in the following section: synthetic calcium indicators and genetically encoded calcium indicators.

3.3 Comparing Synthetic And GECI Calcium Indicators

Synthetic calcium indicators have a few advantages. They are easier to utilize, do not require transfection and have established loading protocols[27]. Synthetic dyes come in a range of binding affinities and spectral ranges and have a wide range of applications for experiments. Currently, popular

synthetic dyes include Oregon green, Calcium green-1, and Fluo-3, among others[27]. Indicators are loaded by pipetting imaging dyes onto the surface of the brain, although the depth of penetration of the indicator depends on several factors, such as health of the animal, type and amount of anesthesia, and the length of time the brain is exposed to the dye[27]. However, while they are easier to load, they provide several disadvantages that can be addressed by genetically encoded calcium indicators.

Genetically encoded calcium indicators (GECI's) are probes that typically contain a fluorescent protein fused to a protein involved in cell signaling[28]. While synthetic molecules are invasive, cannot be targeted, and cannot be used for repeated measurements over time, GECI's can be transfected with minimal invasiveness, can be targeted to specific cell types or components of cells, and can be used for long-term measurements[29].

Fluorescent measurements are typically calculated as $\Delta F/F_0$, or the change in fluorescence intensity relative to the resting intensity[30]. The performance of different GECI's can be compared by calculating signal-to-noise ratios (SNR's). SNR can be calculated as the ratio between fluorescent signal and shot noise over the baseline fluorescence ($\Delta F/N^{-1/2}$), where N is the number of photos detected[31]. Factors affecting GECI performance and SNR include brightness, pH sensitivity, folding sensitivity, and photobleaching of the sensor[32].

GECIs have frequently used to detect neural activity. Action potentials themselves can be difficult to detect due to the short time that they last, but calcium transients can last beyond the short duration of the action potential, making it easier to detect neural activity[33,34]. One of the first applications of GECIs for neural activities was to functionally map the antennal lobe of flies in response to odorant stimuli[16]. GECIs have also been used for long-term studies, such as mapping the tracking the place fields of CA1 pyramidal cell in mice over a series of weeks, which could not be accomplished by synthetic dyes[36].

3.4 GCaMP For Fluorescent Imaging

GCaMP is a particular kind of GECI, widely used in fluorescent imaging. GCaMP consists of green fluorescent protein (GFP), calmodulin (CaM, a calcium binding protein), and an M13 peptide (targets calmodulin)[37].

In GCaMP, circularly permutated GFP is connected at its N terminus to the GFP, while the C terminus is connected to CaM[38]. Calcium binding to CaM causes a conformational shift due to the interaction between CaM and M13, which causes the GFP to fluoresce[39]. GCaMP, without access to calcium, appears to exist in a poorly fluorescent state due to protonation of the chromophore, and the conformational change caused by the binding of calcium eliminates this protonation pathway, leading to brighter and detectable fluorescence[38,40]. Therefore, calcium activity in the brain can cause fluorescence. To capture this fluorescence, different kinds of imaging can be used. Specifically, for our purposes, we can use widefield imaging.

3.5 Advantages Of Widefield Imaging

Different methods are available imaging the mouse brain. Popular among these are two-photon microscopy and widefield imaging. Two-photon microscopy is a nonlinear microscopy technique that allows high resolution for imaging tissues. In particular, two-photon excitation of fluorescence can allow for longer image depths in live animals and tissues[41]. Additionally, two-photon excitation can allow for the creation of optical sections[42]. However, the increased depth and resolution of two-photon microscopy comes at the cost of decreased field of view, giving widefield microscopy an advantage in observing a greater area of the brain when tracking neural dynamics[43]. Widefield microscopy imaging has been used to image much wider areas of the brain, from a range of about 25,000-50,000 neurons available for imaging[44]. Widefield imaging also has the advantage that it can be performed through

intact skull windows, which reduces the need for invasive craniotomies, and is an inexpensive alternative to two-photon microscopy[45].

Widefield imaging with GCaMP has found many uses with neural activity. It has been used to track spontaneous sensory-evoked activity in mice from activated sites to distant, functionally directed in awake and asleep mice[46], show to show neural activity in proper sensory cortices of the brain in response to auditory, visual and mechanical stimuli[47] ,and examine movement generation in the brain on a macro-scale level across different cortices of the brain[48]. Widefield imaging, along with GCaMP, has many advantages in defining neural activity on a larger scale. Long term, we aim to use widefield imaging to image the visual cortex of the brain to observe its response to optical stimuli. However, there are issues that can arise from this.

3.6 Hemodynamics Can Contaminate Fluorescence Data

A recognized issue in the widefield imaging of calcium indicators *in vivo* is the effect of hemodynamics and blood flow on imaging. Specifically, hemodynamic response of the brain to functional stimuli can contaminate calcium signals[47,49]. The contamination happens as a result of neurovascular coupling. Neurovascular coupling refers to the relationship between neural activation and cerebral blood flow, through the coupled actions of neurons, endothelium, and glial cells such as astrocytes and pericytes[49,50]. When the brain is stimulated, increases in blood flow can often be seen after a short delay[51]. Reasons for this increase in blood flow have been attributed to a variety of potential reasons, including a need for more oxygen or glucose in the cell, or a need for waste removal and heat regulation[52]. Capillaries and arterioles have been noted to increase in diameter, while venous oxygenation levels increase due to increased blood flow[52].

Various imaging methods have used neurovascular coupling to their advantage to track hemodynamics of the brain. Techniques such as functional magnetic resonance (fMRI) imaging, blood-

oxygen-level-dependent signals (BOLD) imaging, and intrinsic optical signal (IOS) imaging take advantage of this relationship to use blood flow, volume and oxygenation as a proxy for neural activity[52,53]. IOS imaging in particular converts changes in reflected light intensity into changes in both deoxygenated and oxygenated local hemoglobin concentrations[54]. IOS imaging involves illuminating the surface of the brain with a specific wavelength and converting the changes in reflected light intensity to changes in oxygenated and deoxygenated hemoglobin concentrations.

The contamination of widefield fluorescent imaging results from the presence of endogenous absorbers. Fluorescence excitation and emission can be absorbed by these endogenous absorbers. Among them, hemoglobin is a strong absorber [55]. Hemoglobin absorption of signals can be particularly hard to overcome in part because it is a broad spectrum absorber across both the excitation and emission wavelengths of GCaMP, visualized in Figure 3 below[49].

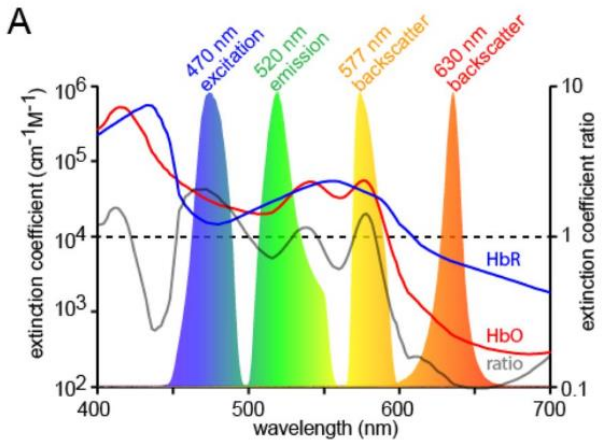

Figure 3: Absorption spectra of oxygenated (HbO) and deoxygenated (HbR) hemoglobin against the excitation and emission peaks of GCaMP fluorescence. Source: Valley et. all[49]

Both oxygenated and deoxygenated hemoglobin can take part in absorption. As stated, when the brain is stimulated, oxygenation levels increase via neurovascular coupling. The increase in oxygenated hemoglobin, through the course of stimulation causes an increase in absorption of the fluorescent signal, as can be seen in the uncorrected data in Figure 4 below.

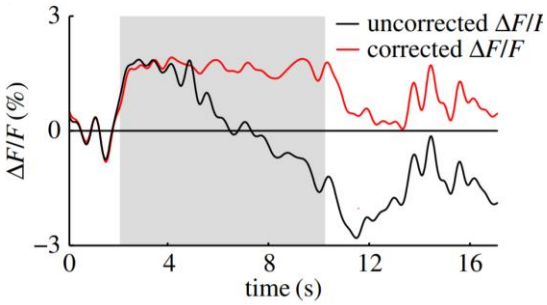

Figure 4: Sample raw fluorescent and corrected data taken from a mouse undergoing hind paw stimulation, showing that left uncorrected, fluorescent signals will decrease over the course of stimulation. Source: Ma et. all[55]

But as seen in the graph, we can also correct for hemodynamic interference. By using an IOS system, the change in oxygenated and deoxygenated hemoglobin concentrations can be calculated. By using these changes to correct the collected fluorescent data, a corrected change in fluorescence graph can be generated. As such, we aim to use the same method of correction on our own fluorescent data to correct signals.

This thesis aims at the development and optimization of an intrinsic optical imaging (IOS) system that, when integrated with a fluorescence widefield imaging system, can be used to calculate the concentration of hemoglobin in the blood, which can then be applied to hemodynamic correction.

3.7 THESIS OBJECTIVES

The original objectives of this thesis were to develop a method by which widefield GCaMP imaging of a mouse cortex could be appropriately corrected by using hemodynamic imaging using an IOS imaging system. The IOS system would first be validated by building and using a piezoelectric system for somatosensory stimulation. The IOS system would then be combined with a fluorescence microscope system and used for cortex imaging of the brain.

The original objectives of the thesis, some of which have had to be revised due to restrictions placed on research due to COVID-19 are as follows:

Objective 1: Piezoelectric Whisker Stimulator Setup (Chapter 4)

This objective involves the construction and completion of a whisker stimulator. Whisker stimulation is a validated method of causing a response in the somatosensory cortex of the brain, and this method will be used to evoke the signals collected by the IOS system.

Objective 2: IOS Setup (Chapter 5)

This objective involves the completion of an IOS imaging system. The first step is to instrument an IOS imaging system. After instrumentation, IOS data will be acquired from a mouse cortex *in vivo* during a resting state. Finally, a MATLAB code will be developed to process the IOS data to obtain hemodynamic signals and covert intensity values into changes in oxygenated and deoxygenated hemoglobin concentration.

Objective 3: Advancing the IOS Analysis (Chapter 6)

Due to restrictions placed on animal experimentation by Brown in light of COVID-19, objective 3 was not able to be completed. While the major scope of the thesis has been kept the same, only the third objective has been shifted onto advanced IOS data analysis. Typical IOS data analysis is done using two

wavelengths (expanded on in Chapter 5 methods). This revised objective focuses on advancing the analysis to instead use three wavelengths to see if more accurate data can be obtained.

Objective 4: Fluorescence microscope construction and Integration of System (revised)

This objective involves construction and completion of a fluorescence microscope system by which GCaMP can be excited, and the emitted fluorescent signals can be detected. Then, the final goal is to integrate the IOS imaging system, the GCaMP imaging system, and the piezoelectric stimulation system together. Both IOS and GCaMP data will be acquired from the somatosensory cortex of a mouse *in vivo* using piezoelectric whisker stimulation. A MATLAB code will be developed to correct the GCaMP fluorescence data using IOS data using calculated hemoglobin concentrations.

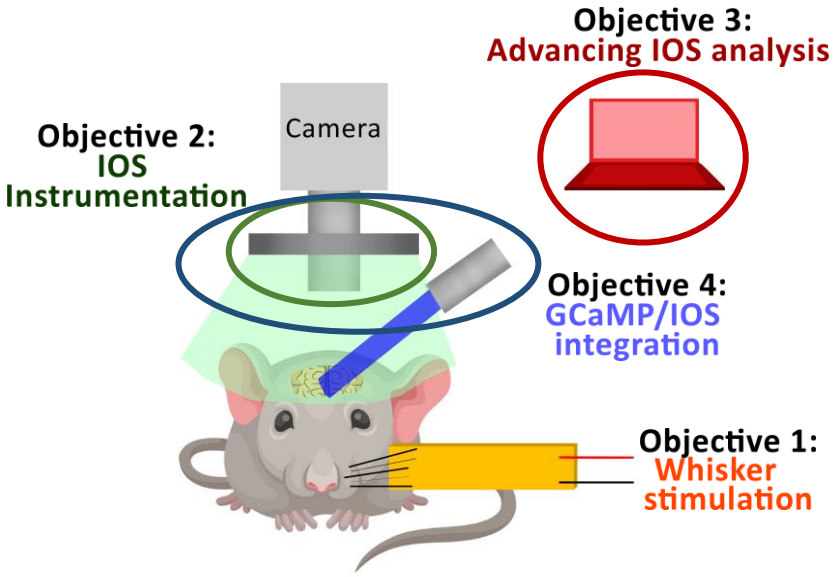

Figure 5: Description of thesis objectives

CHAPTER 4: BUILDING A LOW-COST PIEZOELECTRIC WHISKER STIMULATOR

4 INTRODUCTION

To ultimately prove that NIR light can stimulate the visual cortex of brain, we plan to use a combined GCaMP/IOS imaging system. However, in order to validate the accuracy of this system, we must first test it using a previously validated method of stimulation. Whisker stimulation is a method of mechanical stimulation that has been used in previous studies[56–60]. Whisker contact with an object causes transduction of the force into an action potential firing in sensory neurons[61]. Each whisker transmits displacement to the primary somatosensory cortex by a synaptic pathway, creating a neuronal pathway called the whisker-barrel projection[56]

The piezoelectric stimulator built uses a piezoelectric bender placed in contact with the mouse whisker to deflect the whiskers. Piezoelectric benders transduce electrical energy into mechanical energy. Layers of piezoceramic sheets on either side of the bender contract or expand based on the voltage received, which in turn causes bending of the piezo, detailed in Figure 6.

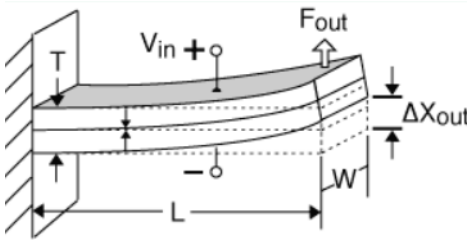

Figure 6: Bending of a two-layered piezo. Source: Piezo.com[62]

Other types of mechanical stimulation do exist, with one cheap alternative being an air puff method. However, this method is difficult to time and control precisely, and delays associated with air movement or decline in pressure over distance must be accounted for[56]. Piezoelectric stimulators allow for much more precise control over stimulation and can be targeted to certain whiskers. This chapter details the development of a low-cost piezoelectric stimulator.

4.1 REQUIREMENTS:

Detailed below are several requirements needed to have an effective piezoelectric stimulation system.

1. *Deflection*: The stimulator must deflect the whiskers enough to cause a stimulus response in the somatosensory cortex
2. *Control*: The stimulator must be controllable and programmable so as to deliver precise stimulations within a certain time point
3. *Signal*: A smooth change in voltage signal (as opposed to a digital signal) must be sent to the stimulator, to prevent damage to the piezoelectric bender
4. *Robustness:* The stimulation system must not by moved by external forces during the experiment (i.e. piezobender forces)
5. *Cost:* The stimulator must be low-cost. Components for a piezoelectric stimulation system can easily be extremely expensive, and so a primary goal was to make the stimulator as cheap as possible

4.2 METHODS

4.2.1 CIRCUIT

PIEZOELECTRIC BENDER

The chosen piezoelectric bender was a compromise between cost and range. Many piezoelectric stimulators that provide a higher range of motion can cost $700+. The chosen bender (Thorlabs PB4NB2W) provides up to 450µm of movement in either direction at a low cost. While a higher amplitude of motion has been noted to provide better data[57], stimulation of the cortex has been observed even using 250µm of movement[56]. While it is possible to move the bender in two directions, for stimulation purposes only one direction of bending was necessary.

PIEZOELECTRIC DRIVER

Benders typically require high voltages to operate. As such, a main component of the circuit is providing enough voltage to the bender. The Thorlabs PB4NB2W requires up to 150V for full range of motion. There were multiple possible power supply options. These included using a high voltage linear DC power supply, a single channel dynamic piezo driver, or using a generic amplifier to achieve the necessary voltage. Different options had different tradeoffs to use. Using a linear DC power supply would require a triggering mechanism or high voltage relay to control the voltage output, and by extension piezo motion. In addition, a high voltage relay typically outputs square waves, which do not provide the smooth change in voltage needed for the piezoelectric bender. Using a generic amplifier presented a cheap but less reliable option. A generic amplifier would not account for piezo-specific needs, such as the accounting for potential for voltage pushback from the piezo. Therefore for its reliability, a single channel dynamic driver was used.

While piezo specific drivers can easily reach up to $1000, the precision they provide was not required for our purposes, so the BD200 piezoelectric driver (Piezo Drive) was used to power our bender. The driver takes a 0-3V input and then converts it into a 0-200V output to the bender. A low-cost benchtop DC linear power supply (TACKLIFE) was used to provide the 24V needed to power the piezoelectric driver.

PIEZOELECTRIC CONTROL

An NiDAQ was used as the input to the piezo driver to allow for precision control of the bender for timing. By using a triangle wave analog output from the DAQ, the voltage could be smoothly ramped from 0-3V. A LabVIEW script was used to control the output from the DAQ to allow for precise timing. The circuit diagram can be seen below.

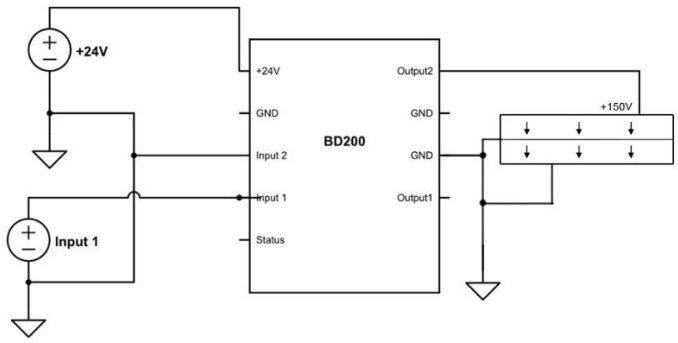

Figure 7: Circuit diagram of piezoelectric stimulator. A 24V power supply powers the BD200 piezo electric driver. A 0-3V input from Input 1 (NiDAQ) is converted by the BD200 to a 0 – 150V output over the top layer of the piezo, which, when the bottom and middle layer are connected to ground, is translated into bending in a single direction.

Finally, the circuit was soldered onto a DOT PCB board so it could be retained permanently for future usage.

4.2.2 FRAMEWORK

The experimental rig was custom designed and 3D printed. Three main components were designed, as can be seen in Figure 6 below.

Component 1: A joint holder for the DOT PCB board and the BD200 driver. The holder allowed for movement of the board without disconnecting wiring/crucial components, while also encapsulating the BD200 driver to minimize human contact with the high voltage components of the device.

Component 2: A holder for the piezoelectric bender. The holder stretched only as far as the inactive area of the bender, so as to prevent interference with the bending elements. The bender was glued onto the holder at its inactive section.

Component 3: A base part, printed to hold the bender in place. In order to keep this base part from moving during stimulation, a second, higher density layer was printed with higher infill to keep the part steady as the piezo moved and attached to the bottom.

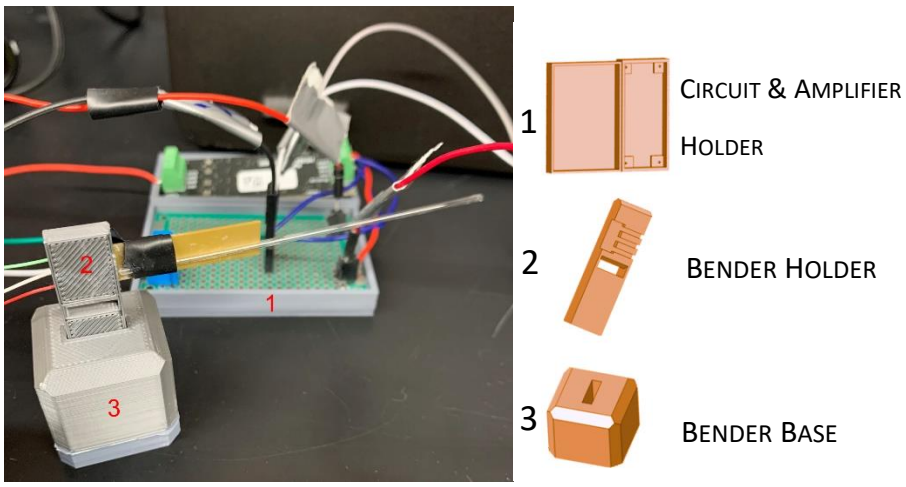

Figure 8: Design of the piezoelectric stimulation system. (1) The holder for the circuit board and the piezoelectric driver, designed to keep both elements steady and in place during experimentation. (2) The piezoelectric bender holder, attached to the bender to allow for bending motion without additional movement. (3) The base, holding the piezoelectric bender up at an appropriate height for it to be attached to the mouse whisker.

For attachment of the mouse whisker to the bender during experimentation, a glass capillary tube was attached to the bender. A thread is inserted through the tube. During experimentation, the thread is looped around the whisker, and then pulled back into the tube for stimulation.

4.3 Cost Breakdown

The total cost (broken down by component in Table 1) of the device is about $250. This can be considered low-cost, considering that a higher-end piezoelectric bender (PICMA® PL127.11/140.11) can cost $400+ and a piezoelectric actuator amplifier (PICMA® LVPZT-Amplifier) can cost as much as $1400+.

Component	Manufacturer	Price
Piezoelectric Bender: Thorlabs PB4NB2W	Thorlabs	$66.84
BD200 Dual-Channel 200V Amplifier	PiezoDrive	$88.00
DOT PCB Board Set	AUSTOR	$16.00
DC Variable Power Supply	TACKLIFE	$67.97
Glass Capillary Tubes	Kimble Chase	$8.95
		Total: $247.76

Table 1: Cost-breakdown of piezoelectric stimulation system.

4.4 Discussion and Conclusions

Piezoelectric whisker stimulation systems have the benefit of precise control and targeting. This section details the construction of a simple, low-cost piezoelectric stimulation system that can be used in conjunction with hemodynamic imaging. We can afford to make the system low-cost because we image the cortex from a more surface level. If a more targeted imaging system (such as two-photon microscopy) was being utilized, or if certain neurons were being targeted for recording, higher precision instrumentation would be necessary. When looking at cost, one item of note is that the NiDAQ and associated LabVIEW program used to control the input signal to the piezoelectric driver had already been purchased by the lab previously, as so was not factored into the costs. If purchasing the NiDAQ was

necessary, that would drive the cost up. However, alternative input signal sources could be explored, as mentioned in Chapter 4.3.1. Another lower cost alternative is to reduce and control power from a power outlet as outlined by Galvez et. all[56]. A rheostat was used to reduce current, while a 5V DC miniature solid state relay was used to gate the voltage, controlled by a LabVIEW program, bypassing the need for both the NiDAQ input and a piezoelectric amplifier, providing a potentially cheaper alternative.

While the piezoelectric whisker stimulation system worked by itself, research restrictions prevented integration and testing with the IOS system. Thus, during experimentation, stimulation frequency, stimulus duration, and amplitude of the signal sent to the piezo (which in turn controls the range of motion of the signal) will need to be optimized to see what allows for the best signals.

5 CHAPTER 5: IOS INSTRUMENTATION AND IMAGING

5.1 INTRODUCTION

Intrinsic optical signal (IOS) imaging is a method by which changes in optical diffuse reflectance of the cortex can be linked to neural activity. When light enters the brain, it scatters, and exits from the same surface to be detected by the camera[55]. When neural activity occurs, the intensity of the reflected light will generally change in the region of the brain where this neural activity is occurring. Part of this absorption has been attributed to the total hemoglobin concentration (HbT), which can itself be split into the changing concentrations of oxygenated (HbO) and deoxygenated (HbR) hemoglobin in the blood[62]. Delivery of oxygen to brain tissues requires the conversion of HbO to HbR, and variations in the concentrations of these two proteins also changes the absorption properties of blood[50].

In IOS imaging, the cortex surface of interest is illuminated with different wavelengths of light to collect intensity data. Due to the different absorption spectra for both oxygenated and deoxygenated hemoglobin, the specific wavelength of light used can have a significant effect on the results received[63]. Certain wavelengths are more preferential to HbO, while others are more preferential to HbR. Green light (530nm) is an isosbestic point in the absorption spectra, such that both HbO and HbR have the same absorption values, making the reflectance data of this wavelength sensitive to changes in total hemoglobin and blood flow. Red light (625nm) is most sensitive to HbR, while blue light (470nm) is more sensitive to HbO[55]. The intensity data collected from these wavelengths can be used to calculate the concentration of HbO and HbR.

This chapter examines the instrumentation of the IOS imaging system and validation of the analysis code. After the IOS system was instrumented imaging was subsequently performed on a resting animal to test the system. Demonstration of how changes in HbO and HbR can be calculated is shown

using previously collected hemodynamic data taken of a mouse stimulated by an air puff whisker stimulation system.

5.2 METHODS

5.2.1 ANALYSIS OF HEMODYNAMIC DATA: BEER'S LAW:

Analysis of hemodynamic data can be done based off a modification of Beer's law. Beer's Law, in a non-scattering medium, can be written as:

$$Equation\ 1: I = I_0 e^{-\mu_a x}$$

Where *I* is the transmitted intensity, and I_0 is the is incident light. The optical path length is *x,* and μ_a is the sample absorption coefficient. However when there is significant scattering in a sample, light attenuation becomes a factor of both the absorption and the scattering[64]. Incident light becomes scattered in the brain, affecting the pathlength of a photon through the medium. Additionally, scattering creates uncertainty as to the spatial properties of a photon of light (i.e. where it entered the brain and where it visited), and affects the photons detected by the camera, as not all emitted photons will be detected in the field of view of the camera due to the spatial redistribution from scattering[55]. This uncertainty, while not precisely quantifiable, can be estimated by a modification on Beer's Law, giving:

$$Equation\ 2: I = I_0 e^{-\mu_a X + G}$$

Here, *X* now represents a scaling of pathlength *x* by some factor to account for the longer distance travelled by the photon, and *G* represents the geometric factors that cause uncertainty in exactly how many of the exiting photons were detected by the camera. *G* can be accounted for by dividing by the intensity at time = 0. Following the methods outlined by Ma et. all (2016)[55], further modifications by accounting for time and wavelength, yields an equation for the absorption coefficient:

$$Equation\ 3: \Delta\mu_A(t,\lambda) = \frac{-1}{X(\lambda)} \ln\left(\frac{I(t,\lambda)}{I_0(t,\lambda)}\right)$$

Here, we have the absorption as a factor of the intensity ratio and pathlength. To connect the absorption factor to the change in hemoglobin concentration, we can look at an alternate form of Beer's Law:

$$A = \varepsilon l c$$

Where *A* is the amount of light absorbed, *l* is the pathlength, ε is the molar extinction coefficient for the absorber, and *c* is the concentration of the absorbing species. This equation can also be written with respect to time as:

$$Equation\ 4: \Delta A(t) = \varepsilon l \Delta c(t)$$

Now, the left-hand term of Equation 3 is equal to the absorbance ($-\ln\left(\frac{I(t,\lambda)}{I_0(t,\lambda)}\right)$), divided by the pathlength (X(λ)). Therefore, we divide the absorbance *A* by pathlength *l* in Equation 4, we arrive at:

$$Equation\ 5: \Delta\mu_A(t,\lambda) = \frac{\Delta A(t,\lambda)}{l} = \varepsilon(\lambda)\Delta c(t)$$

If there are multiple absorbers, as we have in our case (HbR and HbO), then the equation for *N* absorbers becomes:

$$Equation\ 6: \Delta\mu_A(t,\lambda) = \sum_N \varepsilon_N(\lambda)\Delta c_N(t)$$

Because there are two absorbers of value in blood for our purposes, this becomes:

$$Equation\ 7: \Delta\mu_A(t,\lambda) = \varepsilon_{HbO}(\lambda)\Delta c_{HbO}(t) + \varepsilon_{HbR}(\lambda)\Delta c_{HbR}(t)$$

When illuminating with two wavelengths, equations 7 can be split into two equations, one for $\lambda_1 = 70nm$ and another for $\lambda_2 = 530nm$. Solving for our two unknown concentrations with these two equations yields:

$$Equation\ 8a: \Delta c_{HbR}(t) = \frac{\varepsilon_{HbO}(\lambda_{470})\mu_A(t,\lambda_{530}) - \varepsilon_{HbO}(\lambda_{530})\mu_A(t,\lambda_{470})}{\varepsilon_{HbO}(\lambda_{470})\varepsilon_{HbR}(\lambda_{530}) - \varepsilon_{HbO}(\lambda_{530})\varepsilon_{HbR}(\lambda_{470})}$$

$$Equation\ 8b: \Delta c_{HbO}(t) = \frac{\varepsilon_{HbR}(\lambda_{470})\mu_A(t,\lambda_{530}) - \varepsilon_{HbR}(\lambda_{530})\mu_A(t,\lambda_{470})}{\varepsilon_{HbR}(\lambda_{470})\varepsilon_{HbO}(\lambda_{530}) - \varepsilon_{HbR}(\lambda_{530})\varepsilon_{HbO}(\lambda_{470})}$$

We can use equations 8a and 8b with the intensity data collected to calculate these parameters.

5.2.2 Instrumentation

The IOS imaging system was created by fixing a 3-LED controller ring illuminator around a CCD camera. A 3D printed piece was designed to keep the ring in place around the camera. The 3-LED controller was set to illuminate with lights of wavelengths 470nm, 530nm, and 625nm. A LabVIEW program was used to control the illuminator using digital outputs from an NiDAQ.

5.2.3 Image Acquisition

Imaging was performed using a CCD camera at about 30Hz. NiDAQ controls were used to switch sequentially between 470nm, 530nm, and 625nm light (with a 10Hz frame rate for each channel). For data where a stimulus was applied, animal whiskers were stimulated for 5 seconds at a frequency of 5Hz using an air puff system to induce a response in the somatosensory cortex.

5.2.4 Animal Preparation:

The animal was administered 2.5% isoflurane. An area of the skull overlying the somatosensory cortex was shaved, and surgical scrub was applied over incision site to prevent contamination. A 2 cm midline incision was made on the scalp and the skin and both side of the midline was retracted. A 6 mm area of the skull overlying the region of interest of the cortex was thinned with a dental burr until transparent (100 μm thickness). The thinned skull was carefully removed over the region of interest by cutting the thinned skull with scissors, keeping the dura intact. A well was created around the region of interest using dental acrylic, filled with a 1% agarose solution in artificial CSF at the room temperature, and covered with a small glass cover slip. With this window sealed by agarose and covered by the cover slip, the brain was protected from contamination and dehydration. A metal frame was glued by dental acrylic to the exposed skull, used to hold the head and prevent motion during microscopy measurements.

For imaging, the animal was initially administered 3% isoflurane to induce anesthesia, before being placed under the IOS system for *in vivo* imaging. During the imaging session, isoflurane percentage was reduced to 1.5% for the duration of the experiment, administered using a nose cone that held the mouse in place during imaging. Oxygen saturation, pulse rate, and temperature were continuously monitored with pulse oximetry and a rectal probe during the whole surgical procedure and experiment. The body temperature was maintained at 37 °C and the pulse rate remained within the normal range of 250–350 pulse/min. All animal-based experimental procedures were reviewed and approved by the Institutional Animal Care and Use Committee (IACUC) of Brown University and Rhode Island Hospital, according to the guidelines and policies of office of laboratory animal welfare and public health service, National Institutes of Health.

5.2.5 IMAGE PROCESSING

Analysis of images was performed using MATLAB (2018a, MathWorks) on 1288x964 pixel images. The initial data array was split up into three separate arrays, one for each wavelength used for illumination along with their corresponding time points. Each data set had 5 trials (multiple points of stimulation). A baseline response was created by averaging initial frames up until the first point of stimulation. The responses for each of the 5 trials in the experiment were taken and averaged together to create an average stimulus response that was then divided by then divided by the baseline to create the fractional change from the resting point. These fractional changes were equivalent to $\frac{I}{I_o}$. Using Equation 3, we can calculate μ_A at the desired wavelength. Values for the pathlength *X* have been estimated in previous studies using Monte Carlo simulations[65], and the values by wavelength can be found in the methods described by Ma et. all[55]. The values used were: X_{470} = 0.526691 and X_{530} = 0.371713.

Calculated values of μ_A for both wavelengths were used to solve Equations 8a and 8b. Values of molar extinction coefficients from a standardized list were used (units in cm^{-1}/M)[66] :

$$\varepsilon_{HbO}(\lambda_{470}) = 33209.2,\ \varepsilon_{HbR}(\lambda_{470}) = 16156.4,\ \varepsilon_{HbO}(\lambda_{530}) = 39956.8,\ \varepsilon_{HbR}(\lambda_{535}) = 39036.4.$$

Δc_{HbO} and $\Delta c_{HbR}(t)$ was calculated for each pixel, before being averaged to create a mean change in concentration value per absorber for each time point.

5.3 RESULTS

5.3.1 INSTRUMENTATION TESTING: RAW IMAGES

To test the IOS system, images were taken of the somatosensory cortex of the mouse at rest, seen in Figure 9. Images of the brain can be seen, illuminated with 470nm, 530nm, and 625nm light, with vascular structures in black.

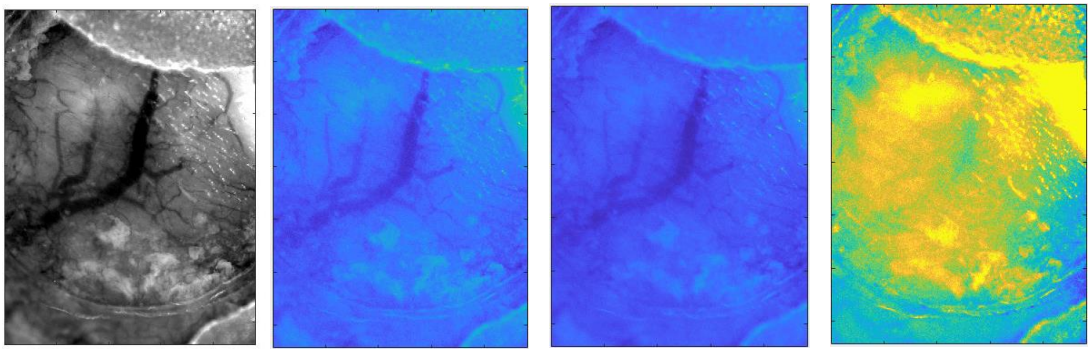

Figure 9: In order: Raw, 470nm, 530nm, and 625nm images of the cortical window of the resting animal, taken as an initial test of the IOS imaging system.

Due to research restrictions placed by COVID19, it was not possible to use the system while stimulating the animal. The proceeding sections examine analysis methods for IOS data collected previously using a different method of whisker stimulation, air puff stimulation.

5.3.2 PROCESSED REFLECTANCE

Reflectance images from both the 470nm and 530nm wavelengths can be seen in Figure 10 below. The raw intensities captured by the camera were processed using the methods described in Section 5.2.5. Areas with darker reflectance correlate to an increase in the concentration of an absorber at that location, which we theoretically assume to be hemoglobin. These concentrations are noted to be generally increasing during and post-stimulus for both wavelengths.

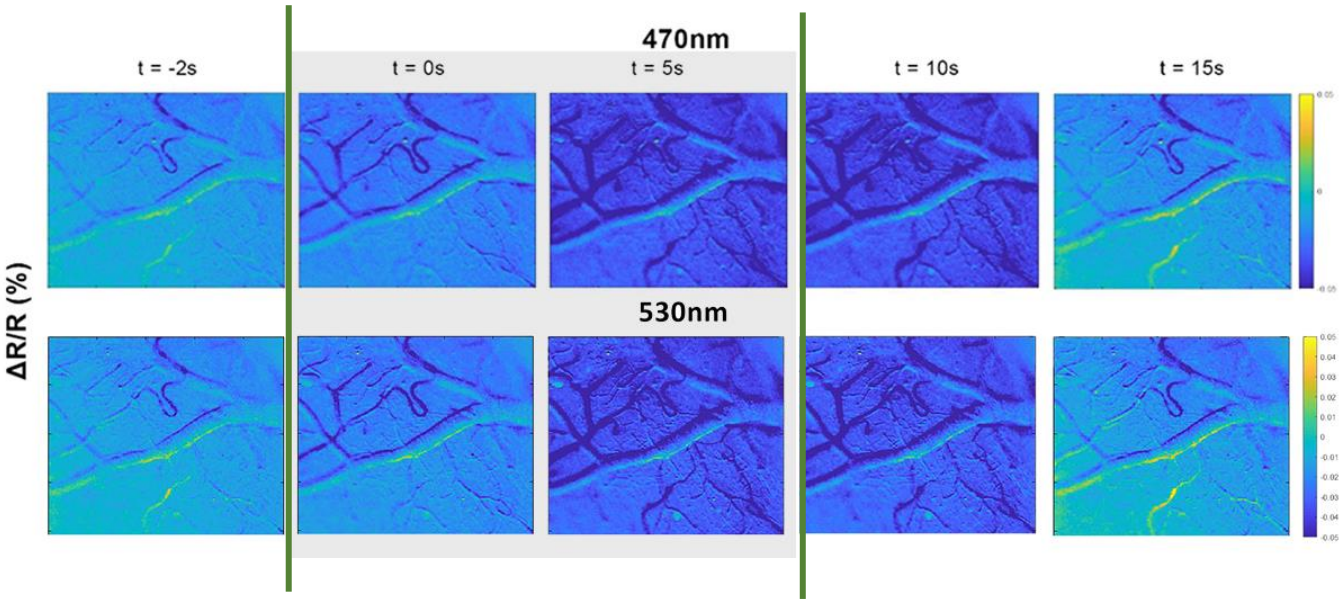

Figure 10: Processed reflectance images for 470nm and 530nm wavelengths. The shaded area between the green lines indicates the duration of stimulation. Percent reflection decreases across stimulus duration.

5.3.3 Determining Hemoglobin Concentrations

Spatial Profile of Hemoglobin Concentration Change

Using the equations described in 5.2.1 and the image processing described in 5.2.5, the reflectance data from Figure 10 can be solved at each pixel for a change in oxygenated hemoglobin concentration (HbO) and a change in deoxygenated hemoglobin concentration (HbR). HbO concentration change is visualized in Figure 11 below. Increases in HbO concentration change were visualized by brighter areas along the maps. Using a spatial profile, certain vascular structures were identified, noted in the figure. Based on literature, structures showing high change in HbO were assumed to be arteries, while structures showing little change in HbO were assumed to be veins[55].

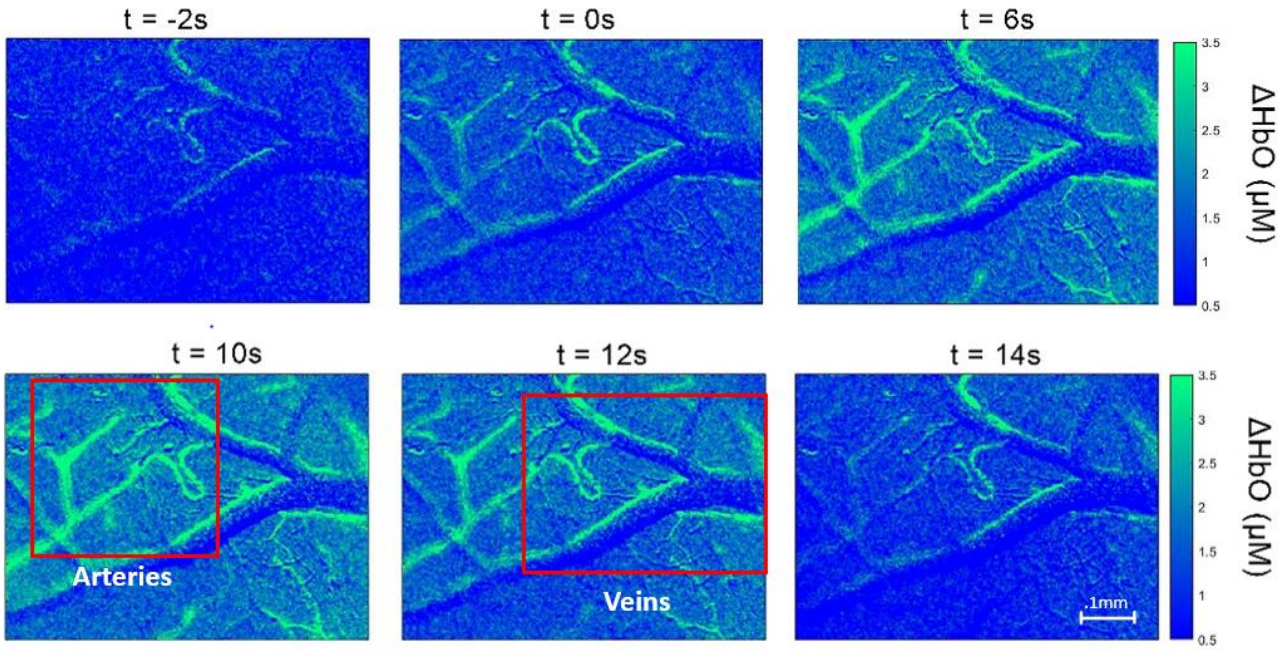

Figure 11: Spatial profile HbO concentration changes, starting from t = -2s, with the stimulus applied at t = 0s. Spatial location of HbO changes can be used to identify arteries and veins, noted in the figure. The peak of HbO concentration occurs at 10s, about 5 seconds after the stimulus is applied.

Visualized changes in HbR concentrations can be seen in Figure 12 below. Slight increases in HbR were seen throughout the course of the experiment. Localized changes in HbR were pinned down in the veins.

However, HbR activity was also noted in the arteries, which was not according to expected behavior, as no change in HbR would be expected in arteries carrying mainly oxygenated blood.

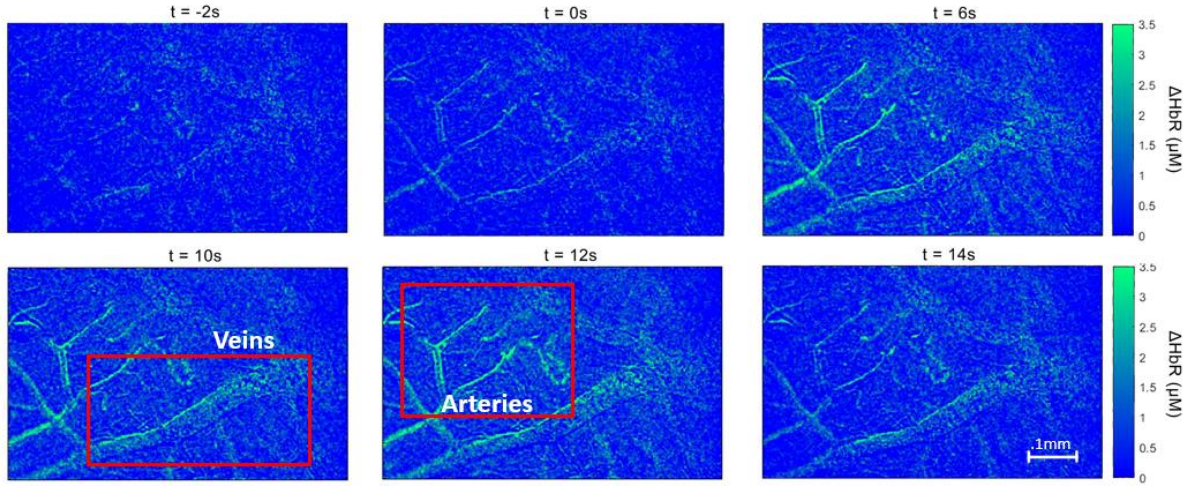

Figure 12: Spatial profile HbR concentration changes, starting from t = -2s, with the stimulus applied at t = 0s. Spatial location of HbO changes can be used to identify arteries and veins, noted in the figure. HbR activity can be visualized, as expected, in the veins. However, HbR activity is also visualized in the arteries, which is atypical.

Temporal Profile of Hemoglobin Concentration Change

The change in concentrations across a spatial profile was averaged at each time point (each individual frame) to create a temporal profile of averaged data, seen in Figure 13 below. During the stimulus period (shaded light grey), we see that hemoglobin concentrations trended upward. HbO (oxygenated hemoglobin) concentrations rose during the stimulus and hit their maximum at t=10s before decreasing again. HbR (deoxygenated hemoglobin) concentrations showed a slight decrease post stimulus before increasing and continuing to rise.

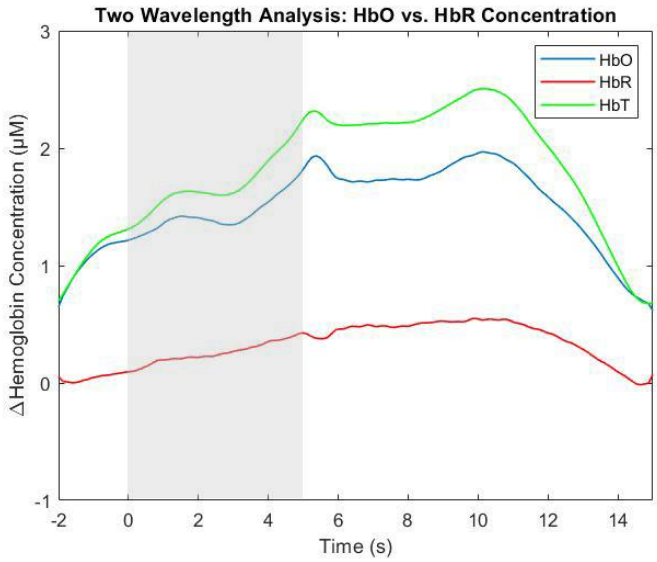

Figure 13: (Left) Raw image of the tested area. Averaged collected intensity values using the 470nm and 530nm wavelengths were used to calculate HbO, HbR, and HbT concentrations. (Right): Calculated hemoglobin concentrations are plotted against the 15 second duration of the experiment using an average of 5 trials. Shaded gray area indicates the time of stimulus (air puff stimulation of the animal whisker, applied for 5 seconds at 5Hz). Data from -2 to 0 seconds was used to create a baseline intensity.

5.4 DISCUSSION

When comparing processed results to expected results, we see promising patterns that validate the analysis process. After stimulation, typical hemoglobin concentration changes show an increase in oxygenated hemoglobin and a decrease in deoxygenated hemoglobin concentration, both changing a short delay after the stimulus is applied, an example of which from literature is shown in Figure 14a below[50,67].

We can see this expected behavior in oxygenated hemoglobin (Fig.9)**.** However, of note is the relative lack of change in deoxygenated hemoglobin concentration. This could be due to physiological data contamination. However, it could also be a function of the specific area imaged. The specific behavior of types of hemoglobin have been shown to vary with the vascular compartment of interest[55]. Arterioles will tend to have larger increases in HbO concentrations with little to no change in HbR concentrations, and diameter increases can cause a change in HbT, an example of which from literature can be seen in Figure 14b below. This behavior is very similar to the analyzed data in Figure 13, which shows large increases in HbO with little change in HbR, suggesting that our imaged field of view likely contained a large artery which contributed significantly to our collected light intensities. While the collected results do not show the same decrease in HbO and HbT concentrations shown in 14b (after the 15 second mark), it should be noted that the time-scale of the figure is 20 seconds, while the collected data was only on a 15 second time scale. If further time was allotted for the experiment, we might have seen a similar response, especially as a downward trend in HbO and HbT changes could be seen at the end of the experiment.

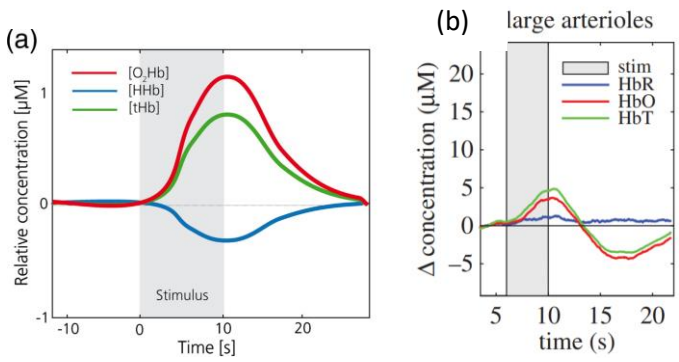

Figure 14: a) Ideal changes in hemoglobin species in response to neurovascular coupling as a result of neural activation. A large increase in HbO can be seen as well as a decrease in HbR. Source: Scholkmann et. all, 2014[68] b) The typical hemodynamic response of a large arteriole in response to neural activation. Large increases in HbO with little change in HbR can be observed, which matches the behavior of the collected data. Source: Ma et. all, 2016[55]

There are some discrepancies between ideal behavior and what was seen, such as the discussed minimal change in HbR. There appears to be some amount of crosstalk between the wavelengths of light. Such crosstalk has been noted in literature and has been thought to be a factor of either incorrect pathlengths, or suboptimal wavelength pairs[71]. As shown in Figures 11 and 12, we see changes in oxygenated hemoglobin and deoxygenated hemoglobin in the same vascular structures, which we would normally not expect to see as vascular structures tend to carry either mainly oxygenated or deoxygenated blood. The much larger increase in HbO suggests that this vascular structure is an artery. It is likely that the change in HbR being noted is actually HbO change being miscalculated as an HbR change, an 'HbO noise' in the results so to speak. The use of the HbO sensitive 470nm wavelength, along with the possibility of a large artery contributing to significant HbO response, could be responsible for the observed noise.

5.5 Conclusions

The result of the resting mouse somatosensory cortex provided an initial demonstration of capability. For examining previously collected data that used an alternate form of whisker stimulation, we used a modified form of Beer's Law to convert the reflectance values collected by the camera into changes in HbO and HbR concentration. Examining the temporal and spatial changes in hemoglobin

concentration, as well as wavelength reflectance data shows consistent trends that, barring some physiological disturbances, match those reported in the literature, validating our analysis process. Future research, when restrictions are lifted, would integrate these two systems and perform the analysis shown above on the data collected using the piezoelectric whisker stimulation system (Objective 4). Ultimately, the concentrations calculated by these methods will be necessary for hemodynamic correction of fluorescent signals.

As was noted, HbO changes seem to dominate the intensities collected from both wavelengths, resulting in HbO noise factoring into HbR changes. Chapter 6 will examine a method by which this HbO noise might be reduced by also including intensity data from 625nm light in our calculations.

6 CHAPTER 6: OPTIMIZING THE IOS ANALYSIS WITH MULTIPLE WAVELENGTHS

6.1 INTRODUCTION

The method of IOS imaging explored in Chapter 5 uses a two wavelength analysis, specifically the 470 and 530nm wavelengths. Minimally, only two wavelengths are required to calculate the change in HbO and HbR concentrations. Some methods have used only the 530nm wavelength to represent HbT concentration changes, though this method is particularly susceptible to alterations of hemodynamic responses by anesthesia and by compromised hyperemic responses[50]. As mentioned, 470nm light is most sensitive to changes in oxygenated hemoglobin, while 530nm light is isosbestic, and therefore equally sensitive to both oxygenated and deoxygenated hemoglobin. As seen in Chapter 5, using just these two wavelengths risks weighting the results towards the concentration of oxygenated hemoglobin, particularly if the deoxygenated hemoglobin response is small. A multiwavelength analysis that also incorporates red light illumination, which is more sensitive to deoxygenated hemoglobin concentrations, could result in more accurate concentrations of oxygenated and deoxygenated hemoglobin. This section details the development and application of a multiwavelength analysis method that incorporates a 625nm wavelength and its potential use in correcting fluorescent signals.

6.2 METHODS

6.2.1 LEAST SQUARES FIT

This method builds on the Beer's Law modification detailed in Chapter 5.2. The modification for multiwavelength analysis from Equation 7, which calculates the absorption coefficient as a factor of wavelength and time states:

$$Equation\ 7: \Delta\mu_A(t,\lambda) = \varepsilon_{HbO}(\lambda)\Delta c_{HbO}(t) + \varepsilon_{HbR}(\lambda)\Delta c_{HbR}(t)$$

When doing a two-wavelength analysis, we can create two equations:

$$Equation\ 9a: \Delta\mu_A(t,\lambda_{470}) = \varepsilon_{HbO}(\lambda_{470})\Delta c_{HbO}(t) + \varepsilon_{HbR}(\lambda_{470})\Delta c_{HbR}(t)$$

$$Equation\ 9b: \Delta\mu_A(t,\lambda_{530}) = \varepsilon_{HbO}(\lambda_{530})\Delta c_{HbO}(t) + \varepsilon_{HbR}(\lambda_{530})\Delta c_{HbR}(t)$$

Equations 9a and 9b can be rewritten as a linear system of equations:

$$\text{Equation 10: } \begin{bmatrix}\Delta\mu_A(t,\lambda_{470})\\ \Delta\mu_A(t,\lambda_{530})\end{bmatrix} = \begin{bmatrix}\varepsilon_{HbO}(\lambda_{470}) & \varepsilon_{HbR}(\lambda_{470})\\ \varepsilon_{HbO}(\lambda_{530}) & \varepsilon_{HbO}(\lambda_{530})\end{bmatrix}\begin{bmatrix}\Delta c_{HbO}(t)\\ \Delta c_{HbR}(t)\end{bmatrix}$$

A third equation for the third wavelength ($\lambda = 625nm$), can then be added to this matrix. This same process would apply to any additional wavelength as well.

$$\text{Equation 11: } \begin{bmatrix}\Delta\mu_A(t,\lambda_{470})\\ \Delta\mu_A(t,\lambda_{530})\\ \Delta\mu_A(t,\lambda_{625})\end{bmatrix} = \begin{bmatrix}\varepsilon_{HbO}(\lambda_{470}) & \varepsilon_{HbR}(\lambda_{470})\\ \varepsilon_{HbO}(\lambda_{530}) & \varepsilon_{HbR}(\lambda_{530})\\ \varepsilon_{HbO}(\lambda_{625}) & \varepsilon_{HbR}(\lambda_{625})\end{bmatrix}\begin{bmatrix}\Delta c_{HbO}(t)\\ \Delta c_{HbR}(t)\end{bmatrix}$$

With three equations and two unknowns, this is an overdetermined system of equations. A least-squares fit, a method of regression analysis, can then be used to approximate the solutions for HbO and HbR concentrations[69].

Molar extinction coefficient values used were $\varepsilon_{HbO}(\lambda_{625})$ = 732, $\varepsilon_{HbR}(\lambda_{625})$ = 5763.4, and X_{625} = .45224. The HbO molar extinction coefficient used was from a table of tabulated values[70]. For the

HbR molar extinction coefficient and the pathlength X_{625} (which is needed to solve for $\mu_A(t, \lambda_{625})$), no published data was available for the 625nm wavelength. However, data was available for 624nm and 626nm wavelengths, and so an average was taken between the available wavelengths for both values.

6.2.2 MATLAB Processing

MATLAB processing was performed according to the methods detailed in Chapter 5 Methods. Average intensity values were calculated for each wavelength by dividing the stimulus response by the baseline response, as mentioned. The resulting three matrices became the starting point for the multiwavelength analysis. The least squares fit calculations was applied across every pixel in the frame. The absorbance for each wavelength at one pixel was moved into a temporary system of matrices, according to Equation 11. A least squares fit was calculated, generating a change in concentration for HbO and HbR, before emptying the array and moving to the next pixel. Change in concentrations for both types of hemoglobin were then added to their own arrays, generating two arrays with concentrations changes. The average concentration change was then calculated for each time frame.

6.2.3 Animal Preparation and Imaging

Animal preparation and imaging for the previously collected data were performed according to the methods detailed in Section 5.2.4.

6.3 Results

6.3.1 625nm Light Reflectance Profiles

A comparison of the reflectivity of all three wavelengths is visualized in Figure 15 below. An increase in reflectance can be visualized across the vein in the 625nm light, marked as a region of interest below. An increase in reflectance can be associated with a decrease in absorber concentration, in this case theoretically the HbR concentration. However, this reflectance can only be visualized on a small scale (0 to .12%). Additionally, for the 625nm light, at t = 5s a marked dip in reflectance in the background around the vasculature can be seen compared to the t = 0s and t = 10s timepoints around it.

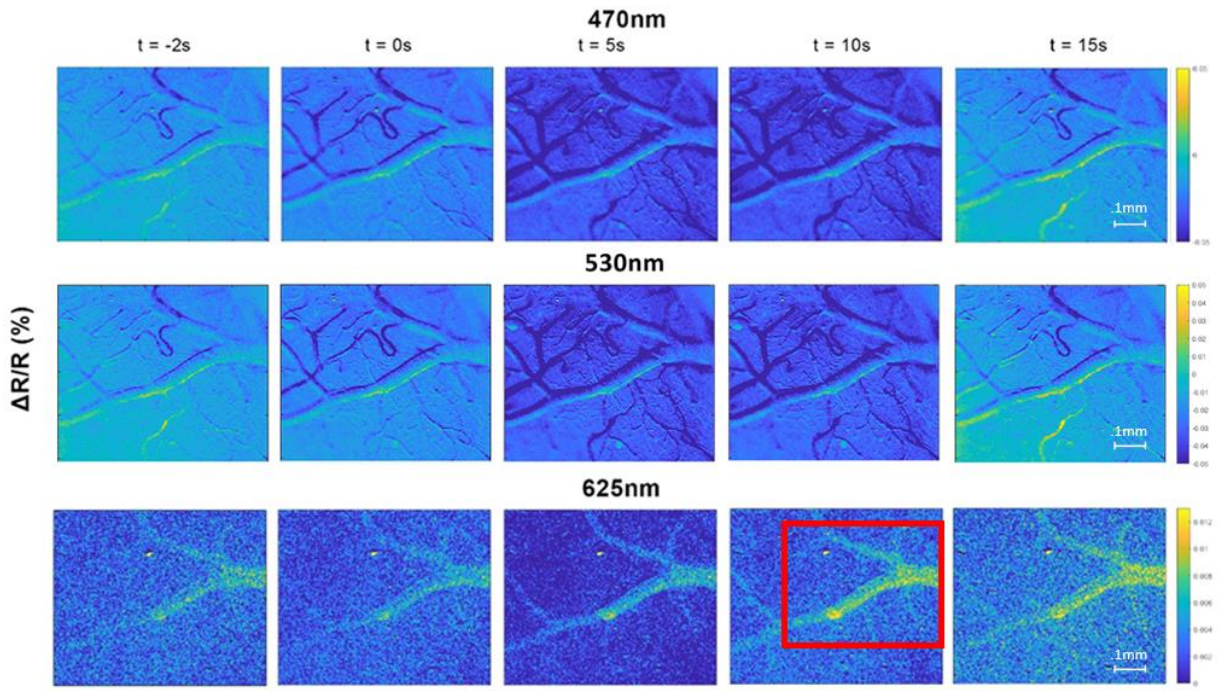

Figure 15: Processed reflectance images for 470nm, 530nm, and 625nm wavelengths. Stimulus was applied at t = 0s for a duration of 5 seconds. An increase in reflectance can be seen for 625nm light in the marked region of interest (red box), and a dip in background reflectance around venous vasculature can be observed in 625nm light at t = 5s.

To further characterize the dip in reflectance noted above, the reflectance profiles of all the wavelengths were plotted temporally by taking the average reflectance at each time point, seen in Figure 16 below. Wavelength reflectance of 625nm light increases over the course of stimulation (marked by the shaded gray area). However, almost directly after the stimulus (t = 5.14s), 625nm reflectance decreases significantly. This dip in 625nm reflectance aligns with a dip in 470nm and 530nm reflectance. As noted in Figure 15 the spatial profile for 625nm light at this time, t = 5s, shows a decrease in background reflectance. As the temporal wavelength is taken as an average of the entire frame, it is likely that increase in reflectance seen in the vein at that point was dominated by the decrease in general background reflectance. Thus, when an average was taken, the background decrease caused the overall average to drastically drop.

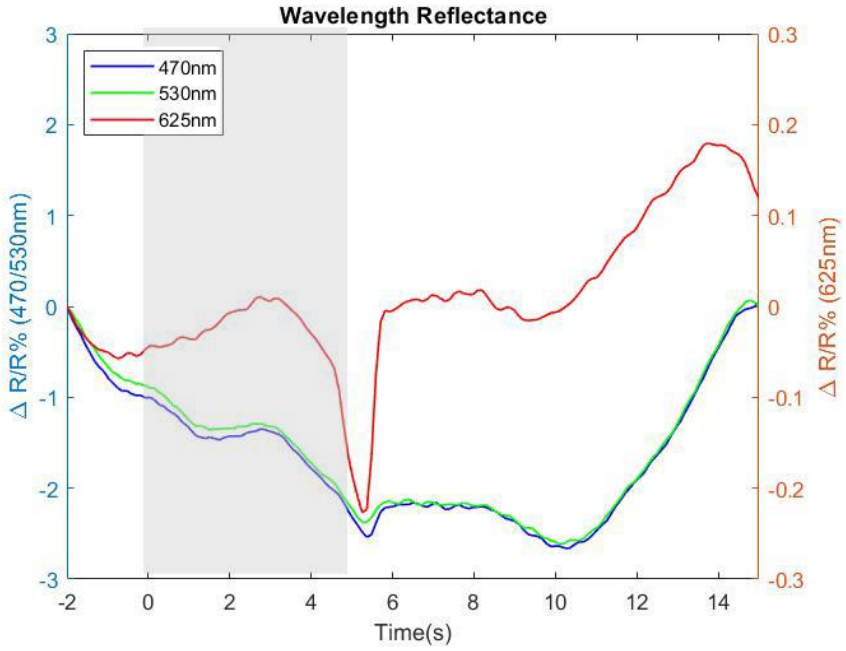

Figure 16: Comparison of reflectance values for three different wavelengths (470nm and 530nm reflectances following the left axes, 625nm reflectance noted on the right axis). During stimulation period, 470nm and 530nm wavelengths show decreasing reflectance, while 625nm wavelength shows increasing reflectance. 625nm reflectance shows a sudden decrease post-stimulus that aligns with dips seen in 470nm and 530nm reflectances as well.

6.3.2 Multiwavelength Method Shows Lower HbR Concentrations

HbO, HbR and HbT concentrations were recalculated using the least-squares method and compared in Figure 17 below to results from the two wavelength analysis method. HbT showed a 5% average decrease in change in concentration using a multiwavelength analysis. A greater shift was seen in the change in HbO concentration, which increased by an average of about 13%. General trends of wavelength activity remain the same in either analysis case.

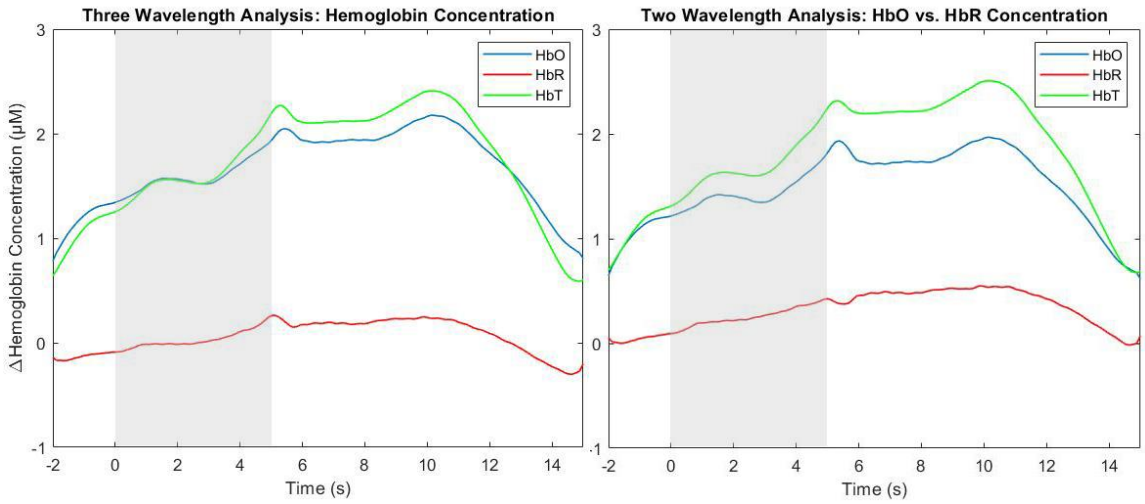

Figure 17: Left: Calculated hemoglobin concentrations using the three wavelength analysis are plotted against the 15 second duration of the experiment. Data from -2 to 0 seconds was used to create a baseline intensity. Right: Calculated hemoglobin concentrations using the two wavelength analysis detailed in Section 5 methods for comparison. An average of 5 trials was used for each. While general trends remain the same between both kinds of analyses, differences in trends can be seen when looking at increased HbO concentrations, and a decrease in HbR concentration

More notable changes can be seen examining HbR concentrations. As seen in Figure 18 below, HbR concentrations are lower overall when calculated with a three wavelength analysis. Figure 18 shows a comparison between calculated HbR concentration changes using a two and three wavelength analysis method. While a post-stimulus spike can be seen in both analyses (at t = 5s), the multiwavelength method showed a sharper peak and subsequent drop compared to the two wavelength method. With the two wavelength method, HbR concentration displayed a sharp increase in concentration again at around the t= 6s mark and continued to rise post-stimulus. In comparison, the three wavelength method did not show this sharp increase and did not show the general rise in HbR concentration seen with the two wavelength method.

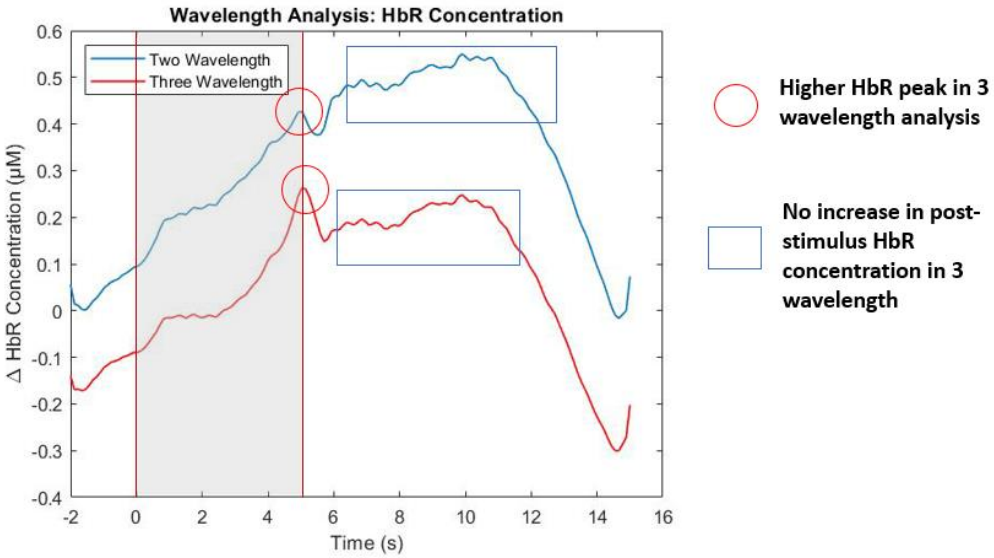

Figure 18: A comparison between HbR concentration change trends between a two and three-wavelength analysis. Areas showing different behavior are noted. Overall HbR concentration changes are lower when calculated with the three-wavelength analysis method. The end-of-stimulus peak is higher in the HbR change calculated by the three-wavelength analysis. HbR wavelengths in a two wavelength analysis show a post stimulus increase that is not calculated by the three wavelength analysis. Shaded area indicates whisker stimulation of animal (duration of 5 seconds, frequency of 5Hz)

The changes in HbR concentration can be represented by a spatial profile. Figure 19 visualizes the spatial profile of HbR concentration changes at three timepoints for both methods of analysis. The two wavelength analysis shows widespread HbR concentration changes. However, in the three wavelength analysis, HbR change is much more localized to the venous structures.

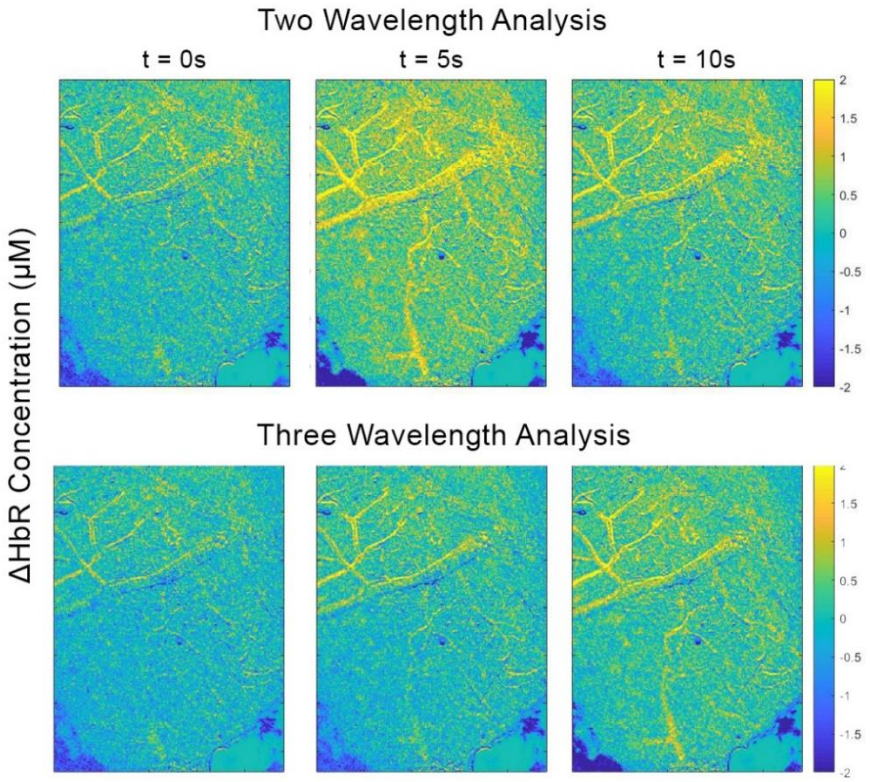

Figure 19: Spatial profile of change in HbR concentrations calculated from a two wavelength analysis method (top row) and a three wavelength analysis (bottom row), at time points t = 0s (stimulus start), t = 5s (stimulus end) and t = 10s (HbO concentration peak). When using 3 wavelength analysis, vasculature shows overall smaller increases in HbR concentrations.

6.4 DISCUSSION

6.4.1 625nm wavelength absorption shows sensitivity to changes in deoxygenated hemoglobin concentrations

The value of including a third wavelength in hemodynamic data analysis can be first established by the showing the sensitivity of the 625nm wavelength to HbR concentrations. As noted in Figure 15, there was an increase in reflectance of 625nm light in venous vascular structures throughout the course of the experiment. Physiologically, we expect to see a decrease in HbR concentration in venous structures as oxygenated blood rushes into the system. The rise in 625nm light reflectance, specifically over the vein throughout the course of the experiment, signifies a decrease in HbR concentration across the vascular structure. However we do not see a decrease in HbR concentration with a temporal profile for either analysis method, even though we can visualize a decrease in concentration with the spatial profile. As noted, 625nm reflectance changes could only be visualized on an extremely small scale, suggesting that red light is poorly absorbed by the cortex. The 625nm reflectance change in response to HbR concentration change could also have been overshadowed by reflectance change in response to much stronger HbO concentration changes (explored further in 6.4.3).

6.4.2 Using a 625nm wavelength reduces the dominating effect of HbO concentration changes

Using the three wavelength analysis, HbR concentration changes are overall lower. Additionally, these concentrations do not increase post-stimulus, as noted in Figure 18. When examining the HbR changes spatially in Figure 19, we see a marked decrease in general HbR levels using a three wavelength analysis. In the two wavelength analysis, we can see the HbO noise discussed in Section 5.5. However, inclusion of the HbR sensitive wavelength dramatically decreases the amount of HbO noise seen throughout the three wavelength spatial profile. Although changes in HbR concentration can still be seen in some arteriole structures, the magnitude of the change is also reduced. HbR changes are also noted to be more localized to venous structures where changes would expect to be seen. The increase spatial accuracy suggests that the averaged temporal concentration changes for HbR are also likely to be

more accurate. Additionally, with less HbO noise the HbR concentrations will overall be smaller, as was observed in the results, which also likely brought it closer to the true HbR concentration levels.

As mentioned, the two wavelength analysis in Figure 18 shows that HbR continues to increase post-stimulus, behavior that is not observed in the three wavelength analysis. However, this increase occurs along with an increase in HbO concentration changes, which happens as an influx of oxygenated blood rushes into the system. Therefore, the reason this increase is seen is likely to be that as HbO concentration changes increase, the amount of HbO noise factored into HbR changes in the two wavelength analysis increases as well, which will cause the HbR concentration change to increase, resulting in the observed behavior post-stimulus. However, when this HbO noise is filtered out with the 3 wavelength analysis, its effect on HbR concentrations becomes much less prominent. The behavior we see of HbR concentrations not rising post-stimulus in the three wavelength analysis is then likely a more accurate representation of true HbR behavior. Overall, including the 625nm wavelength into the analysis clears up much of the observed HbO noise, leaving what is likely a much more accurate representation of HbR concentration changes.

6.4.3 625nm absorption values can be affected by changes in oxygenated hemoglobin concentrations

Although light of 605-630nm is much more sensitive to HbR concentrations, literature shows that it can be sensitive to HbO concentrations as well[55,67,71–73]. We can also see this represented in the data, particularly in reflectance profiles. As noted in Figure 16, a dip in 625nm reflectance can be observed post-stimulus that aligns with a dip in HbO concentration change. Given the decrease in background reflectance of 625nm at t = 5s in Figure 15, it is likely that this background reflectance change decrease is due to the increase in oxygenated blood, which was detected by the 625nm light.

This sensitivity can have further effects on our calculated oxygenated and deoxygenated hemoglobin concentrations. The three-wavelength analysis calculated a larger peak in HbR

concentrations at the end of the stimulus than we see using a two-wavelength analysis (Fig. 18). This larger increase aligns with an increase in HbO concentrations at that time point (Fig. 17). It is possible that the rise in HbR concentration was due to the increased HbO concentration absorbing the 625nm light. This would also explain why three-wavelength calculated values of HbO were an average of 13% higher than two-wavelength calculated values, because they were bolstered by 625nm light sensitivity.

While this sensitivity might call into question whether we should include a 625nm light in our analysis, we can see that, despite an increase in calculated oxygenated hemoglobin concentrations, there was an overall decrease in HbT, suggesting a significant enough decrease in calculated HbR concentration to counteract the bolstered HbO concentration. The decrease in total hemoglobin concentration brings the results closer in line with the results that we would ideally expect to see.

6.5 Conclusions

Ultimately, we can see that that multiwavelength analysis of hemodynamic data can make a more accurate difference in concentration results calculated, even within the limitations of the data set available. It is essential to not only examine the temporal profile of concentration changes and reflectance changes, but also the spatial profiles as well. We see that 625nm in this case shows poor absorption, given the low reflectance changes. Future experimentation would have to explore whether this absorbance can be increased by either imaging a different area of the somatosensory cortex, or whether changing the stimulation method would have any effect on deoxygenated blood flow. It is possible that a stronger stimulus, such as the piezoelectric whisker stimulator discussed in Chapter 4, would produce a stronger change in deoxygenated hemoglobin that could be detected by the camera.

7 CONCLUSIONS

The aim of this thesis was to work towards the development of a method to obtain accurate fluorescent signals from the animal cortex. Although research restrictions prevented the final objective from being completed, the first two objectives and another revised objective were completed. To accurately correct fluorescent signals from imaging the animal cortex, three components are necessary, a widefield GCaMP microscope, an IOS imaging system, and a method of stimulation. While ultimately the integrated system will be used to demonstrate the potential for NIR light to stimulate the visual cortex, a literature-validated method of stimulation was first needed to validate integrated GCaMP/IOS system.

A robust, controllable piezoelectric whisker stimulation system was designed to provide precise stimulation for IOS and GCaMP imaging, with the aim of providing strong, reliable signals to collect data from. Using an IOS imaging system, the concentrations of hemoglobin that are necessary to correct fluorescent signals can be calculated. The analysis methods developed can generate both spatial and temporal profiles from the changes in oxygenated and deoxygenated hemoglobin concentrations. By using a least-squares fit estimation, a multiwavelength analysis can be performed on collected data. While 625nm light shows low reflectance and is susceptible to absorption by oxygenated hemoglobin, accounting for this HbR sensitive wavelength in an integrated system could allow for better correction of fluorescent signals.

The next steps would be to integrate the piezoelectric whisker stimulator with the IOS imaging system and optimize stimulation parameters until strong signals can be collected for data. Once this is achieved, the IOS system can also be integrated with the GCaMP fluorescence imaging system. The concentration values calculated by the methods outlined in this thesis can be applied to fluorescence microscopy data to correct for hemodynamic interference. Ultimately, these methods will serve as a

critical means in validating a novel method of optical stimulation, to show the promise of an effective retinal prosthetic.

8 REFERENCES

1. Chan C. Molecular pathology of inflammation in age-related macular degeneration. *Acta Ophthalmol (Copenh)*. 2012;90:0-0. doi:10.1111/j.1755-3768.2012.3241.x

2. Bowes Rickman C, Farsiu S, Toth CA, Klingeborn M. Dry Age-Related Macular Degeneration: Mechanisms, Therapeutic Targets, and Imaging. *Investig Opthalmology Vis Sci*. 2013;54(14):ORSF68. doi:10.1167/iovs.13-12757

3. Bhutto I, Lutty G. Understanding age-related macular degeneration (AMD): Relationships between the photoreceptor/retinal pigment epithelium/Bruch's membrane/choriocapillaris complex. *Mol Aspects Med*. 2012;33(4):295-317. doi:10.1016/j.mam.2012.04.005

4. Prevalence of Age-Related Macular Degeneration in the United States. *Arch Ophthalmol*. 2004;122(4):564. doi:10.1001/archopht.122.4.564

5. Coleman HR, Chan C-C, Ferris FL, Chew EY. Age-related macular degeneration. *The Lancet*. 2008;372(9652):1835-1845. doi:10.1016/S0140-6736(08)61759-6

6. Haller J. Risk Factors For Age-related Macular Degeneration And Choroidal Neovascularization. In: Lim J, ed. *Age-Related Macular Degeneration, Second Edition*. Informa Healthcare; 2002. doi:10.1201/9780203909157.ch20

7. Sobrin L, Seddon JM. Nature and nurture- genes and environment- predict onset and progression of macular degeneration. *Prog Retin Eye Res*. 2014;40:1-15. doi:10.1016/j.preteyeres.2013.12.004

8. US Census Bureau. Demographic Turning Points for the United States. Demographic Turning Points for the United States. https://www.census.gov/library/publications/2020/demo/p25-1144.html. Accessed February 25, 2020.

9. Wong WL, Su X, Li X, et al. Global prevalence of age-related macular degeneration and disease burden projection for 2020 and 2040: a systematic review and meta-analysis. *Lancet Glob Health*. 2014;2(2):e106-e116. doi:10.1016/S2214-109X(13)70145-1

10. Rein DB. Forecasting Age-Related Macular Degeneration Through the Year 2050: The Potential Impact of New Treatments. *Arch Ophthalmol*. 2009;127(4):533. doi:10.1001/archophthalmol.2009.58

11. Brody BL, Gamst AC, Williams RA, et al. Depression, visual acuity, comorbidity, and disability associated with age-related macular degeneration. *Ophthalmology*. 2001;108(10):1893-1900. doi:10.1016/S0161-6420(01)00754-0

12. Rein DB, Saaddine JB, Wittenborn JS, et al. Cost-effectiveness of Vitamin Therapy for Age-Related Macular Degeneration. *Ophthalmology*. 2007;114(7):1319-1326. doi:10.1016/j.ophtha.2006.10.041

13. Hau VS, London N, Dalton M. The Treatment Paradigm for the Implantable Miniature Telescope. *Ophthalmol Ther*. 2016;5(1):21-30. doi:10.1007/s40123-016-0047-5

14. Hudson HL, Stulting RD, Heier JS, et al. Implantable Telescope for End-Stage Age-related Macular Degeneration: Long-term Visual Acuity and Safety Outcomes. *Am J Ophthalmol*. 2008;146(5):664-673.e1. doi:10.1016/j.ajo.2008.07.003

15. Brown GC, Brown MM, Lieske HB, Lieske PA, Brown KS, Lane SS. Comparative Effectiveness and Cost-Effectiveness of the Implantable Miniature Telescope. *Ophthalmology*. 2011;118(9):1834-1843. doi:10.1016/j.ophtha.2011.02.012

16. Riazi-Esfahani M, Maghami M, Sodagar A, Lashay A, Riazi-Esfahani H. Visual prostheses: The enabling technology to give sight to the blind. *J Ophthalmic Vis Res*. 2014;9(4):494. doi:10.4103/2008-322X.150830

17. Weiland JD, Humayun MS. Visual Prosthesis. *Proc IEEE*. 2008;96(7):1076-1084. doi:10.1109/JPROC.2008.922589

18. Wells J, Kao C, Mariappan K, et al. Optical stimulation of neural tissue in vivo. *Opt Lett*. 2005;30(5):504. doi:10.1364/OL.30.000504

19. Eom K, Byun KM, Jun SB, Kim SJ, Lee J. Theoretical Study on Gold-Nanorod-Enhanced Near-Infrared Neural Stimulation. *Biophys J*. 2018;115(8):1481-1497. doi:10.1016/j.bpj.2018.09.004

20. Russell JT. Imaging calcium signals in vivo: a powerful tool in physiology and pharmacology. *Br J Pharmacol*. 2011;163(8):1605-1625. doi:10.1111/j.1476-5381.2010.00988.x

21. Grienberger C, Konnerth A. Imaging Calcium in Neurons. *Neuron*. 2012;73(5):862-885. doi:10.1016/j.neuron.2012.02.011

22. Gerard J, Borst G, Helmchen F. [20] Calcium influx during an action potential. In: *Methods in Enzymology*. Vol 293. Ion Channels Part B. Academic Press; 1998:352-371. doi:10.1016/S0076-6879(98)93023-3

23. Kerr JND, Plenz D. Action Potential Timing Determines Dendritic Calcium during Striatal Up-States. *J Neurosci*. 2004;24(4):877-885. doi:10.1523/JNEUROSCI.4475-03.2004

24. Tsien RY. Fluorescent Probes of Cell Signaling. *Annu Rev Neurosci*. 1989;12(1):227-253. doi:10.1146/annurev.ne.12.030189.001303

25. Helmchen F, Waters J. Ca2+ imaging in the mammalian brain in vivo. *Eur J Pharmacol*. 2002;447(2):119-129. doi:10.1016/S0014-2999(02)01836-8

26. Galizia CG, Joerges J, Küttner A, Faber T, Menzel R. A semi-in-vivo preparation for optical recording of the insect brain. *J Neurosci Methods*. 1997;76(1):61-69. doi:10.1016/S0165-0270(97)00080-0

27. Paredes RM, Etzler JC, Watts LT, Lechleiter JD. Chemical Calcium Indicators. *Methods San Diego Calif*. 2008;46(3):143-151. doi:10.1016/j.ymeth.2008.09.025

28. Miyawaki A. Innovations in the Imaging of Brain Functions using Fluorescent Proteins. *Neuron*. 2005;48(2):189-199. doi:10.1016/j.neuron.2005.10.003

29. Pologruto TA, Yasuda R, Svoboda K. Monitoring Neural Activity and [Ca2+] with Genetically Encoded Ca2+ Indicators. *J Neurosci*. 2004;24(43):9572-9579. doi:10.1523/JNEUROSCI.2854-04.2004

30. Macleod GT. Imaging and Analysis of Nonratiometric Calcium Indicators at the Drosophila Larval Neuromuscular Junction. *Cold Spring Harb Protoc*. 2012;2012(7):pdb.prot070110. doi:10.1101/pdb.prot070110

31. Yasuda R, Nimchinsky EA, Scheuss V, et al. Imaging Calcium Concentration Dynamics in Small Neuronal Compartments. *Sci STKE*. 2004;2004(219):pl5-pl5. doi:10.1126/stke.2192004pl5

32. Tian L, Hires SA, Looger LL. Imaging Neuronal Activity with Genetically Encoded Calcium Indicators. *Cold Spring Harb Protoc*. 2012;2012(6):pdb.top069609. doi:10.1101/pdb.top069609

33. Lin MZ, Schnitzer MJ. Genetically encoded indicators of neuronal activity. *Nat Neurosci*. 2016;19(9):1142-1153. doi:10.1038/nn.4359

34. Koester HJ, Sakmann B. Calcium dynamics associated with action potentials in single nerve terminals of pyramidal cells in layer 2/3 of the young rat neocortex. *J Physiol*. 2000;529(Pt 3):625-646. doi:10.1111/j.1469-7793.2000.00625.x

35. Wang JW, Wong AM, Flores J, Vosshall LB, Axel R. Two-Photon Calcium Imaging Reveals an Odor-Evoked Map of Activity in the Fly Brain. *Cell*. 2003;112(2):271-282. doi:10.1016/S0092-8674(03)00004-7

36. Ziv Y, Burns LD, Cocker ED, et al. Long-term dynamics of CA1 hippocampal place codes. *Nat Neurosci*. 2013;16(3):264-266. doi:10.1038/nn.3329

37. Akerboom J, Chen T-W, Wardill TJ, et al. Optimization of a GCaMP Calcium Indicator for Neural Activity Imaging. *J Neurosci*. 2012;32(40):13819-13840. doi:10.1523/JNEUROSCI.2601-12.2012

38. Crystal Structures of the GCaMP Calcium Sensor Reveal the Mechanism of Fluorescence Signal Change and Aid Rational Design. https://www.jbc.org/lens/jbc/284/10/6455#content/figure_reference_1. Accessed March 15, 2020.

39. Nakai J, Ohkura M, Imoto K. A high signal-to-noise Ca 2+ probe composed of a single green fluorescent protein. *Nat Biotechnol*. 2001;19(2):137-141. doi:10.1038/84397

40. Wang Q, Shui B, Kotlikoff MI, Sondermann H. Structural basis for Calcium Sensing by GCaMP2. *Struct Lond Engl 1993*. 2008;16(12):1817-1827. doi:10.1016/j.str.2008.10.008

41. Benninger RKP, Piston DW. Two-Photon Excitation Microscopy for the Study of Living Cells and Tissues. *Curr Protoc Cell Biol Editor Board Juan Bonifacino Al*. 2013;0 4:Unit-4.1124. doi:10.1002/0471143030.cb0411s59

42. Amor R, McDonald A, Trägårdh J, et al. Widefield Two-Photon Excitation without Scanning: Live Cell Microscopy with High Time Resolution and Low Photo-Bleaching. *PLOS ONE*. 2016;11(1):e0147115. doi:10.1371/journal.pone.0147115

43. Yoshida E, Terada S-I, Tanaka YH, et al. In vivo wide-field calcium imaging of mouse thalamocortical synapses with an 8 K ultra-high-definition camera. *Sci Rep*. 2018;8(1):1-15. doi:10.1038/s41598-018-26566-3

44. Kim TH, Zhang Y, Lecoq J, et al. Long-Term Optical Access to an Estimated One Million Neurons in the Live Mouse Cortex. *Cell Rep*. 2016;17(12):3385-3394. doi:10.1016/j.celrep.2016.12.004

45. Silasi G, Xiao D, Vanni MP, Chen ACN, Murphy TH. Intact skull chronic windows for mesoscopic wide-field imaging in awake mice. *J Neurosci Methods*. 2016;267:141-149. doi:10.1016/j.jneumeth.2016.04.012

46. Mohajerani MH, Chan AW, Mohsenvand M, et al. Spontaneous cortical activity alternates between motifs defined by regional axonal projections. *Nat Neurosci*. 2013;16(10):1426-1435. doi:10.1038/nn.3499

47. Allen WE, Kauvar IV, Chen MZ, et al. Global Representations of Goal-Directed Behavior in Distinct Cell Types of Mouse Neocortex. *Neuron*. 2017;94(4):891-907.e6. doi:10.1016/j.neuron.2017.04.017

48. Makino H, Ren C, Liu H, et al. Transformation of Cortex-wide Emergent Properties during Motor Learning. *Neuron*. 2017;94(4):880-890.e8. doi:10.1016/j.neuron.2017.04.015

49. Valley MT, Moore MG, Zhuang J, et al. Separation of hemodynamic signals from GCaMP fluorescence measured with wide-field imaging. *J Neurophysiol*. 2019;123(1):356-366. doi:10.1152/jn.00304.2019

50. Hillman EMC. Optical brain imaging in vivo: techniques and applications from animal to man. *J Biomed Opt*. 2007;12(5):051402. doi:10.1117/1.2789693

51. Ma Y, Shaik MA, Kozberg MG, et al. Resting-state hemodynamics are spatiotemporally coupled to synchronized and symmetric neural activity in excitatory neurons. *Proc Natl Acad Sci*. 2016;113(52):E8463-E8471. doi:10.1073/pnas.1525369113

52. Hillman EMC. Coupling Mechanism and Significance of the BOLD Signal: A Status Report. *Annu Rev Neurosci*. 2014;37:161-181. doi:10.1146/annurev-neuro-071013-014111

53. Santisakultarm TP, Kersbergen CJ, Bandy DK, Ide DC, Choi S-H, Silva AC. Two-photon imaging of cerebral hemodynamics and neural activity in awake and anesthetized marmosets. *J Neurosci Methods*. 2016;271:55-64. doi:10.1016/j.jneumeth.2016.07.003

54. White BR, Bauer AQ, Snyder AZ, Schlaggar BL, Lee J-M, Culver JP. Imaging of Functional Connectivity in the Mouse Brain. *PLoS ONE*. 2011;6(1). doi:10.1371/journal.pone.0016322

55. Ma Y, Shaik MA, Kim SH, et al. Wide-field optical mapping of neural activity and brain haemodynamics: considerations and novel approaches. *Philos Trans R Soc B Biol Sci*. 2016;371(1705). doi:10.1098/rstb.2015.0360

56. Galvez R, Weiss C, Cua S, Disterhoft J. A novel method for precisely timed stimulation of mouse whiskers in a freely moving preparation: Application for delivery of the conditioned stimulus in trace

eyeblink conditioning. *J Neurosci Methods*. 2009;177(2):434-439. doi:10.1016/j.jneumeth.2008.11.002

57. Shin H, Moore CI. Persistent Gamma Spiking in SI Nonsensory Fast Spiking Cells Predicts Perceptual Success. *Neuron*. 2019;103(6):1150-1163.e5. doi:10.1016/j.neuron.2019.06.014

58. Walker JL, Monjaraz-Fuentes F, Pedrow CR, Rector DM. Precision rodent whisker stimulator with integrated servo-locked control and displacement measurement. *J Neurosci Methods*. 2011;196(1):20-30. doi:10.1016/j.jneumeth.2010.12.008

59. Arabzadeh E, Panzeri S, Diamond ME. Whisker Vibration Information Carried by Rat Barrel Cortex Neurons. *J Neurosci*. 2004;24(26):6011-6020. doi:10.1523/JNEUROSCI.1389-04.2004

60. Modified Sensory Processing in the Barrel Cortex of the Adult Mouse After Chronic Whisker Stimulation | Journal of Neurophysiology. https://journals.physiology.org/doi/full/10.1152/jn.00338.2006?url_ver=Z39.88-2003&rfr_id=ori:rid:crossref.org&rfr_dat=cr_pub%3dpubmed. Accessed March 25, 2020.

61. Auffret M, Ravano VL, Rossi GMC, Hankov N, Petersen MFA, Petersen CCH. Optogenetic Stimulation of Cortex to Map Evoked Whisker Movements in Awake Head-Restrained Mice. *Neuroscience*. 2018;368:199-213. doi:10.1016/j.neuroscience.2017.04.004

62. Malonek D, Grinvald A. Interactions between electrical activity and cortical microcirculation revealed by imaging spectroscopy: implications for functional brain mapping. *Science*. 1996;272(5261):551-554. doi:10.1126/science.272.5261.551

63. Bouchard MB, Chen BR, Burgess SA, Hillman EMC. Ultra-fast multispectral optical imaging of cortical oxygenation, blood flow, and intracellular calcium dynamics. *Opt Express*. 2009;17(18):15670-15678.

64. Baker WB, Parthasarathy AB, Busch DR, Mesquita RC, Greenberg JH, Yodh AG. Modified Beer-Lambert law for blood flow. *Biomed Opt Express*. 2014;5(11):4053-4075. doi:10.1364/BOE.5.004053

65. Kohl M, Lindauer U, Royl G, et al. Physical model for the spectroscopic analysis of cortical intrinsic optical signals. *Phys Med Biol*. 2000;45(12):3749–3764. doi:10.1088/0031-9155/45/12/317

66. Tabulated Molar Extinction Coefficient for Hemoglobin in Water. https://omlc.org/spectra/hemoglobin/summary.html. Accessed March 26, 2020.

67. Renaud RN, Martin C, Gurden H, Pain F. <!-- *** Custom HTML *** -->Multispectral reflectance imaging of brain activation in rodents: methodological study of the differential path length estimations and first *in vivo* recordings in the rat olfactory bulb. *J Biomed Opt*. 2012;17(1):016012. doi:10.1117/1.JBO.17.1.016012

68. Scholkmann F, Kleiser S, Metz AJ, et al. A review on continuous wave functional near-infrared spectroscopy and imaging instrumentation and methodology. *NeuroImage*. 2014;85:6-27. doi:10.1016/j.neuroimage.2013.05.004

69. 4.1.4.1. Linear Least Squares Regression. https://www.itl.nist.gov/div898/handbook/pmd/section1/pmd141.htm. Accessed March 30, 2020.

70. Takatani S, Graham MD. Theoretical Analysis of Diffuse Reflectance from a Two-Layer Tissue Model. *IEEE Trans Biomed Eng*. 1979;BME-26(12):656-664. doi:10.1109/TBME.1979.326455

71. Boas DA, Dale AM, Franceschini MA. Diffuse optical imaging of brain activation: approaches to optimizing image sensitivity, resolution, and accuracy. *NeuroImage*. 2004;23:S275-S288. doi:10.1016/j.neuroimage.2004.07.011

72. Bahar S, Suh M, Zhao M, Schwartz TH. Intrinsic optical signal imaging of neocortical seizures: the 'epileptic dip.' *NeuroReport*. 2006;17(5):499–503. doi:10.1097/01.wnr.0000209010.78599.f5

73. Kura S, Xie H, Fu B, Ayata C, Boas DA, Sakadžić S. Intrinsic optical signal imaging of the blood volume changes is sufficient for mapping the resting state functional connectivity in the rodent cortex. *J Neural Eng*. 2018;15(3):035003. doi:10.1088/1741-2552/aaafe4